# Preparation of Mesoporous Mn–Ce–Ti–O Aerogels by a One-Pot Sol–Gel Method for Selective Catalytic Reduction of NO with NH$_3$

Yabin Wei [1], Shuangling Jin [1,*], Rui Zhang [1,*], Weifeng Li [1], Jiangcan Wang [1], Shuo Yang [1], He Wang [1], Minghe Yang [1], Yan Liu [1], Wenming Qiao [2], Licheng Ling [2] and Minglin Jin [1]

[1] School of Materials Science and Engineering, Shanghai Institute of Technology, Shanghai 201418, China; 176081103@mail.sit.edu.cn (Y.W.); 176081107@mail.sit.edu.cn (W.L.); 176082112@mail.sit.edu.cn (J.W.); 176082108@mail.sit.edu.cn (S.Y.); 186081133@mail.sit.edu.cn (H.W.); 186081138@mail.sit.edu.cn (M.Y.); lyan@sit.edu.cn (Y.L.); jml@sit.edu.cn (M.J.)

[2] State Key Laboratory of Chemical Engineering, East China University of Science and Technology, Shanghai 200237, China; qiaowm@ecust.edu.cn (W.Q.); lchling@ecust.edu.cn (L.L.)

\* Correspondence: jinshuangling@sit.edu.cn (S.J.); zhangrui@sit.edu.cn (R.Z.)

check for updates

**Abstract:** Novel Mn–Ce–Ti–O composite aerogels with large mesopore size were prepared via a one-pot sol–gel method by using propylene oxide as a network gel inducer and ethyl acetoacetate as a complexing agent. The effect of calcination temperature (400, 500, 600, and 700 °C) on the NH$_3$–selective catalytic reduction (SCR) performance of the obtained Mn–Ce–Ti–O composite aerogels was investigated. The results show that the Mn–Ce–Ti–O catalyst calcined at 600 °C exhibits the highest NH$_3$–SCR activity and lowest apparent activation energy due to its most abundant Lewis acid sites and best reducibility. The NO conversion of the MCTO-600 catalyst maintains 100% at 200 °C in the presence of 100 ppm SO$_2$, showing the superior resistance to SO$_2$ poisoning as compared with the MnO$_x$–CeO$_2$–TiO$_2$ catalysts reported the literature. This should be mainly attributed to its large mesopore sizes with an average pore size of 32 nm and abundant Lewis acid sites. The former fact facilitates the decomposition of NH$_4$HSO$_4$, and the latter fact reduces vapor pressure of NH$_3$. The NH$_3$–SCR process on the MCTO-600 catalyst follows both the Eley–Rideal (E–R) mechanism and the Langmuir–Hinshelwood (L–H) mechanism.

**Keywords:** Mn–Ce–Ti–O composite aerogel; mesopore size; NH$_3$–SCR; apparent activation energy; SO$_2$ resistance

## 1. Introduction

Nitrogen oxides (NO$_x$), as major air pollutants from the combustion of fossil fuels, cause serious environmental problems, such as acid rain, photochemical smog, and ozone depletion [1,2]. At present, many denitration technologies have been developed to remove NO$_x$ to meet stringent legislation requirements, such as selective catalytic reduction (SCR) [1–6], selective non-catalytic reduction (SNCR) [7], and absorption [8], among which the selective catalytic reduction with NH$_3$ (NH$_3$–SCR) is one of the most promising approaches for NO$_x$ removal owing to its high denitration efficiency and relatively low cost. Vanadium–titanium catalysts are the most commonly used catalysts currently in industry to remove NO$_x$ from stationary sources, including V$_2$O$_5$–WO$_3$/TiO$_2$ and V$_2$O$_5$–WO$_3$(MoO$_3$)/TiO$_2$ [9–12]. However, to satisfy the working conditions of the V-based catalysts, the current SCR denitration device has to be installed upstream of the electrostatic precipitator and the desulfurization device to avoid the deactivation of catalysts by high-concentration fly ash, alkali metals, and SO$_2$ [13], to increase the life time of the catalysts and to reduce the operating costs of denitration.

In addition, the V-based catalysts have some inevitable disadvantages, such as the toxicity of $VO_x$, a narrow operating temperature window (300–400 °C), and a low $N_2$ selectivity [6,14,15]. Therefore, it is of great practical importance to develop catalysts with high catalytic activity and good $SO_2$ resistance under low-temperature conditions (<200 °C).

The $MnO_x$–based catalysts have been considered as promising candidates for NO removal by the $NH_3$–SCR method owing to their inherent environmentally benign nature and superior catalytic activity [13–21]. As an additive, $CeO_2$ can further enhance the catalytic activity of $MnO_x$ in the low temperature range because of its unique oxygen storage capacity and redox performance [22,23]. In addition, $CeO_2$ can enhance the $SO_2$ tolerance of $MnO_x$–based catalysts, because $CeO_2$ can preferentially react with $SO_2$ to reduce the sulfation of $MnO_x$ at the expense of the active $CeO_2$ component [24]. Extensive efforts have also been made to further improve the $SO_2$ resistance of $MnO_x$–$CeO_2$ catalysts, such as inhibiting the $SO_2$ adsorption/oxidation and enhancing the adsorption of active intermediate species by introducing functional promoters [25]. Due to the relatively weak interaction between $TiO_2$ and $SO_2$, $TiO_2$ can act as a protective constituent to inhibit the adsorption of $SO_2$; especially, the coating of a $TiO_2$ shell on $MnO_x$–$CeO_2$ is demonstrated to be a good method to improve the $SO_2$ resistance of the catalysts [1,26]. Moreover, modification with Co, Ni, Fe, and Zn can increase the formation of nitrate species and $NO_2$ on the surface of the $MnO_x$–$CeO_2$ catalysts, thereby enhancing the $SO_2$ resistance [4,13,27]. In addition, it is proved that the pore texture also plays an important role in $SO_2$ resistance of the catalysts [28–31]. Soh et al. suggested that the increase of pore size and specific surface area for $V_2O_5/Al_2O_3$ catalysts can reduce the deactivation rate of active sites [29]. Similarly, Guo et al. investigated the $SO_2$ tolerance of $Fe_2O_3/SBA$-15 catalysts with different pore sizes and found that the decomposition temperature of $NH_4HSO_4$ on the catalyst surface decreased by 40 °C when the pore size of the SBA-15 support increased from 4.8 to 11.8 nm, due to the fact that a larger pore size can produce a higher vapor pressure, thus facilitating the decomposition of $NH_4HSO_4$ [30]. Ma et al. also found that the hollow-structured $CeO_2$–$TiO_2$ catalyst exhibited a better $SO_2$ resistance when it had a larger cavity [31].

At present, the $MnO_x$–$CeO_2$–$TiO_2$ catalysts are prepared by several approaches, including the hydrothermal [26], sol–gel [24], wet impregnation [32] and co-precipitation methods [33], which show good low-temperature $NH_3$–SCR performance. However, the catalytic activities in the presence of $SO_2$ are still limited, probably due to their relatively small pore size. In this work, Mn–Ce–Ti–O composite aerogels with larger mesoporous pore sizes were prepared via a one-pot sol–gel method followed by calcination at different temperatures from 400 to 700 °C. The $NH_3$–SCR catalytic activities with and without $SO_2$ and $H_2O$ were investigated. The mechanisms were discussed based on the characterization results of X-ray diffraction (XRD), $N_2$ adsorption, X-ray photoelectron spectroscopy (XPS), $H_2$–temperature programmed reduction ($H_2$–TPR), $NH_3$–temperature programmed desorption ($NH_3$–TPD), and in-situ diffuse reflectance infrared Fourier transform spectra (DRIFTS).

## 2. Materials and Methods

### 2.1. Catalyst Preparation

The Mn–Ce–Ti–O composite aerogel was prepared via a one-pot sol-gel method by using propylene oxide as a network gel inducer and ethyl acetoacetate as a complexing agent. The molar ratios of (Ti + Mn + Ce) to propylene oxide and ethyl acetoacetate were 1:5.5 and 1:0.3, respectively. Specific steps were as follows. Ethyl acetoacetate was added dropwise to 95 mL of anhydrous ethanol at a rate of 1 drop/s under magnetic stirring, and the mixed solution was put in an ice bath. Then, 0.1 mol of $TiCl_4$ was added dropwise to the above solution by a syringe, and 0.04 mol of $Mn(NO_3)_2 \cdot 4H_2O$ and 0.007 mol of $Ce(NO_3)_3 \cdot 6H_2O$ were added with consecutive stirring until they were completely dissolved. Finally, propylene oxide was added dropwise under continuous stirring for 30 min to obtain a yellow transparent sol. The sol was poured into an ampule (30 mL), sealed, aged in a 30 °C water bath for 2 days, and then aged in a 70 °C water bath for 5 days to obtain a wet gel. The wet gel was

subjected to solvent displacement with n-hexane for 12 h, followed by supercritical drying in n-hexane at 240 °C and 6.0 MPa for 1 h with a heating rate of 1 °C min$^{-1}$·to obtain the precursor of Mn–Ce–Ti–O composite aerogel. The precursor aerogel was calcined at 400, 500, 600, and 700 °C for 3 h with a heating rate of 5 °C min$^{-1}$, respectively, to obtain the Mn–Ce–Ti–O composite aerogels, which were denoted as MCTO-x, where x represents the calcination temperatures.

## 2.2. Catalyst Characterization

The thermal stability of the MCTO-0 was tested by thermogravimetry-differential scanning calorimetry (TG–DSC) on a Netzsch STA 449 analyzer under air from room temperature to 800 °C with a heating rate of 10 °C min$^{-1}$. The XRD patterns of samples were examined on a D/max 2200PC diffractometer using Cu K$\alpha$ radiation as the source ($\lambda$ = 0.15406 nm) with a 2$\theta$ range of 5–80° at a scan rate of 8°·min$^{-1}$. The N$_2$ adsorption-desorption curves were tested to analyze the specific surface area and pore texture of the samples at 77 K on a Micrometrics ASAP 2020 apparatus. Prior to each test, the samples were degassed at 200 °C for 12 h under vacuum. The specific surface area was calculated using the Brunauer–Emmett–Teller (BET) equation, and the pore size distribution and pore volume were calculated based on the density function theory (DFT) model. The morphology of samples was observed by scanning electron microscopy (SEM) with a FEI Quanta 200 FEG microscope. The XPS spectra of the samples were obtained on a Thermo Fisher Scientific ESCALAB 250Xi system using Al K$\alpha$ as the radiation source at 300 W under ultrahigh vacuum (8 × 10$^{-8}$ Pa). The C1s peak (284.8 eV) was used as a standard to calibrate the precise binding energy of Mn 2p, Ce 3d, Ti 2p, and O 1s. The H$_2$–TPR and NH$_3$–TPD experiments were performed on a Micrometrics AutoChem II 2920 instrument; 100 mg of samples were firstly pretreated at 200 °C for 1 h in an Ar atmosphere with a total flow rate of 30 mL·min$^{-1}$, and then cooled to 50 °C. For H$_2$–TPR, the pretreated catalysts were heated to 800 °C in a 10 vol. % H$_2$/Ar mixture gas (30 mL·min$^{-1}$) at a heating rate of 10 °C min$^{-1}$. The H$_2$ consumption of the reduction process was recorded by a thermal conductivity detector (TCD). For NH$_3$–TPD, the pretreated samples were placed in a mixture gas of NH$_3$/Ar (10 vol. % of NH$_3$) with a total flow rate of 50 mL·min$^{-1}$ for 1 h until saturation to ensure a sufficient adsorption of NH$_3$ on the catalyst surfaces. Then pure N$_2$ was blown in for 30 min to remove the non-adsorbed NH$_3$. Finally, the samples were placed in an He atmosphere with a flow rate of 50 mL·min$^{-1}$ to carry out NH$_3$ desorption at a heating rate of 10 °C min$^{-1}$ from 50 °C to 800 °C to obtain the NH$_3$–TPD curves. The in-situ DRIFTS were collected on an FTIR spectrometer (Thermo Fisher Nicolet iZ10) equipped with a smart collector and an MCT/A detector that was cooled by liquid nitrogen. Before each test, the catalysts were pretreated at 350 °C for 2 h under N$_2$ with a flow rate of 50 mL·min$^{-1}$ and cooled down to 200 °C. The background spectrum was collected in N$_2$ atmosphere and automatically deducted from the sample spectrum. In the transient NH$_3$–SCR performance experiment, the MCTO-600 catalyst was firstly exposed to 500 ppm of NH$_3$ (or 500 ppm of NO + 5 vol. % O$_2$) stream for 30 min at 200 °C, then purged with He for 30 min, and finally subjected to 500 ppm of NO + 5 vol. % O$_2$ (or 500 ppm of NH$_3$) to obtain the time-varying DRIFTS. All spectra were collected by accumulating 32 scans at a resolution of 4 cm$^{-1}$.

## 2.3. Catalytic Activity Measurement

The NH$_3$–SCR activity of catalysts was evaluated by a fixed-bed reactor (id: 7.5 mm), in which 0.5 mL of catalysts with 40–80 mesh was fixed by quartz sand (40–60 mesh) and glass wool. The feed-gas consisted of 500 ppm NO, 500 ppm NH$_3$, 5 vol. % O$_2$, 5 vol. % H$_2$O (when used), 100 ppm SO$_2$ (when used), and N$_2$ balance, with a total flow rate of 120 mL·min$^{-1}$, corresponding to the gas hourly space velocity (GHSV) of 14,400 h$^{-1}$. The catalyst reaction temperature was controlled from 120 to 320 °C with a heating rate of 5 °C min$^{-1}$ from 20 °C to the reaction temperatures and held for 30 min to reach a steady state for data collection. The concentrations of NO and NO$_2$ were measured by the chemiluminescence method with an Eco Physics CLD 62s NO/NO$_x$ analyzer, and the concentration of N$_2$O was detected by gas chromatography using a Techcomp GC 7900 apparatus.

The NO conversion (x) and the $N_2$ selectivity (S) were calculated using the Equations (1) and (2), respectively [6,9].

$$x = \frac{[NO]_{in} - [NO]_{out}}{[NO]_{out}} \times 100\% \tag{1}$$

$$S = \left(1 - \frac{[N_2O]_{out}}{[NO_x]_{in} - [NO_x]_{out}}\right) \times 100\% \tag{2}$$

where $[NO]_{in}$ signifies the inlet concentration of NO, $[NO]_{out}$ stands for the outlet concentration of NO, and $[N_2O]_{out}$ is the outlet concentration of $N_2O$.

In addition, in order to better evaluate the catalytic activity of Mn–Ce–Ti–O aerogels, a steady state kinetics investigation on these catalysts was conducted. The calculation of the reaction rate constant $K$ ($cm^3 \cdot g^{-1} \cdot s^{-1}$) is based on the assumption that $[NH_3]$ is a zero-order reaction and $[NO]$ is a first-order reaction [2,34]. The $K$ is calculated by the Equation (3):

$$K = \frac{-V \ln(1-x)}{w} \tag{3}$$

where $K$ is the reaction rate constant ($cm^3 \cdot g^{-1} \cdot s^{-1}$), $V$ means the total flow rate ($mL \cdot min^{-1}$) of the simulated flue gas, $w$ represents the mass (g) of the catalyst, and $x$ is the NO conversion. The apparent activation energy could be obtained by using the Arrhenius equation, as given by Equation (4) as follows:

$$K = K_0 e^{\frac{-E_a}{RT}} \tag{4}$$

where $E_a$ represents the apparent activation energy of catalysts, which could be calculated from the slope of the $ln(K)$ versus 1000/T curves.

To compare the intrinsic activity of the catalysts at different calcination temperatures, turnover frequency (TOF) was calculated using Equation (5) [14,35]. TOF represents the number of NO conversion at a single active site (Mn atom) per unit time; its value is a measure of the catalytic reaction rate on a catalyst. In general, the calculation of TOF requires the conversion of a reactant to be at a relatively low level (<15%) [36,37]. Reaction conditions were as follows: T = 160, 180, 200, or 220 °C, 500 ppm of NO, 500 ppm of $NH_3$, 5 vol. % of $O_2$, balance $N_2$, total flow rate = 240 $mL \cdot min^{-1}$, GHSV $\approx$ 200,000 $h^{-1}$.

$$TOF = \frac{(PV/RT)x}{w \times \beta_{Mn}/M_{Mn}} \tag{5}$$

where $P$, $V$, $R$, $T$, $x$, $w$, $\beta_{Mn}$, and $M_{Mn}$ represents the standard atmospheric pressure (101 KPa), the NO flow rate (0.12 $mL \cdot min^{-1}$), the gas constant (8.314 $J \cdot mol^{-1} \cdot K^{-1}$), the reaction temperature (K), the NO conversion at each temperature, the mass of the catalyst (0.02 g), the atomic percentage of Mn on the surface of the catalyst by XPS, and the relative atomic mass of Mn (54.94 $g \cdot mol^{-1}$), respectively.

## 3. Results and Discussion

### 3.1. Catalyst Characterization

The TG–DSC curve of the MCTO-0 aerogel under air was tested to study its thermal decomposition behavior, which contained three mass loss stages, as shown in Figure 1. The first mass loss stage below 120 °C with an exothermic peak at 86 °C was due to the desorption of adsorbed water. The second mass loss stage in the range of 120–400 °C with two exothermic peaks at 330 °C and 392 °C was detected, which could be attributed to the removal of organic matter and the decomposition of metal oxide precursor. In addition, an endothermic peak at 456 °C was observed for the third mass loss step from 400 to 600 °C. There were mass loss and mass gain involved at this step. The former was caused by carbon burn-off in the temperature range of 400–600 °C, which was 8.2 wt % (from XPS results), and the latter was from the oxidation of $Mn_3O_4$ to $Mn_2O_3$ ($2Mn_3O_4 + 1/2O_2 = 3Mn_2O_3$), which was 3.5 wt %. Therefore, a mass loss was observed at this step.
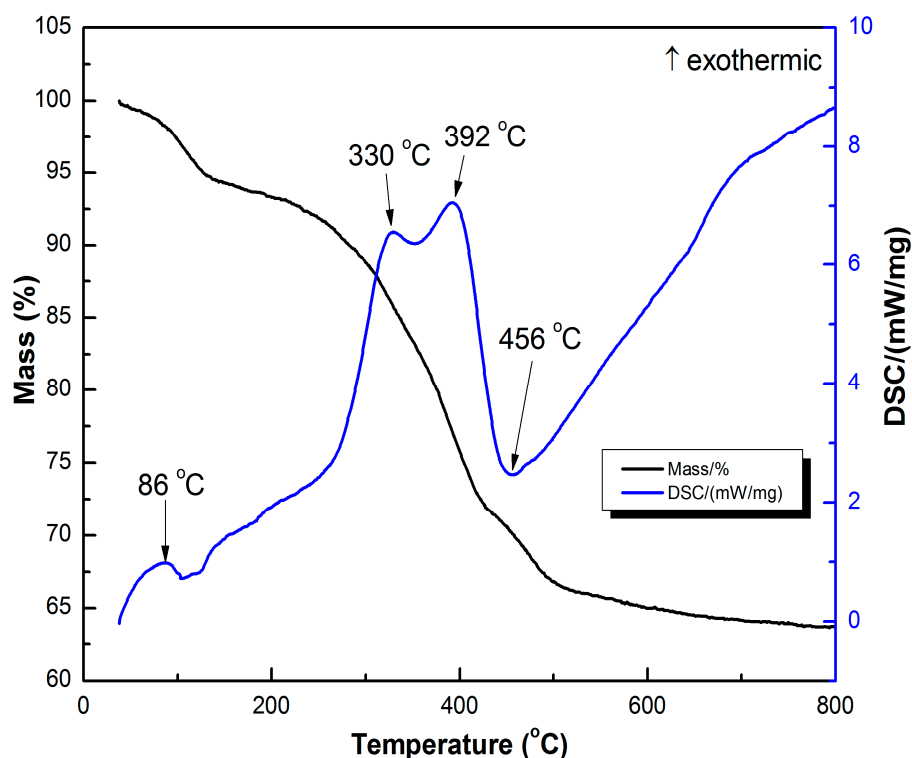
**Figure 1.** Thermogravimetry–differential scanning calorimetry (TG–DSC) curve of sample MCTO-0.

The XRD patterns of the MCTO-0, MCTO-400, MCTO-500, MCTO-600, and MCTO-700 are shown in Figure 2. The diffraction peaks at 25.3°, 37.8°, 38.6°, 48.1°, 51.0°, 55.1°, 62.7°, 68.9°, 70.3°, and 75.3° were observed for MCTO-0 sample, which were attributed to anatase $TiO_2$ (JCPDS 21-1272) [11]. The characteristic peaks of the $Mn_3O_4$ phase (JCPDS 24-0734) at 28.9°, 32.3°, 38.0°, and 59.8° and the $Mn_2O_3$ phase (JCPDS 33-0900) at 32.3°, 35.6°, and 62.3° were detected for the calcined products [38]. In addition, the diffraction peaks for the $CeO_2$ phase with a cubic fluorite structure (JCPDS 34-0394) at 28.8°, 48.2°, and 56.7° appeared for samples MCTO-600 and MCTO-700 [4]. The mean crystallite sizes of the above different phases were calculated using the Scherrer formula, as shown in Table 1; it could be seen that the increase of calcination temperature resulted in the gradual increase in crystallite sizes for the above metal oxides. Significantly, according to the results of below XPS and $H_2$–TPR, $MnO_2$ species were found on the surface of all samples. However, one could not see any standard peaks ascribed to $MnO_2$ in XRD patterns, suggesting that they were highly dispersed on the catalyst surface, which could be beneficial to the $NH_3$–SCR activity.

To gain insight into the pore structure of the obtained catalysts, the $N_2$ adsorption-desorption isotherms of the catalysts were examined, as shown in Figure 3a. All the isotherms exhibited a typical IV-type curve with an H3 hysteresis loop, suggesting the existence of mesoporous pores [39]. In addition, a high nitrogen uptake at high relative pressure over 0.95 was observed for all the samples, indicating the existence of macropores [40], in accordance with the bimodal pore size distributions displayed in Figure 3b. The smaller pores may have been formed by the primary nanoparticles and the larger pores by the secondary particles as a result of aggregation of the primary nanoparticles. With increases in the calcination temperature, the sintering of primary nanoparticles occurred, leading to their gradual disappearance. The secondary particles were relatively stable with increasing calcination temperature, but an apparent decrease of larger pores formed by secondary particles was found at 700 °C, indicating that sintering of the secondary particles occurred. This was why the $NH_3$–SCR activity of the MCTO-700 was lower than that of the MCTO-600.
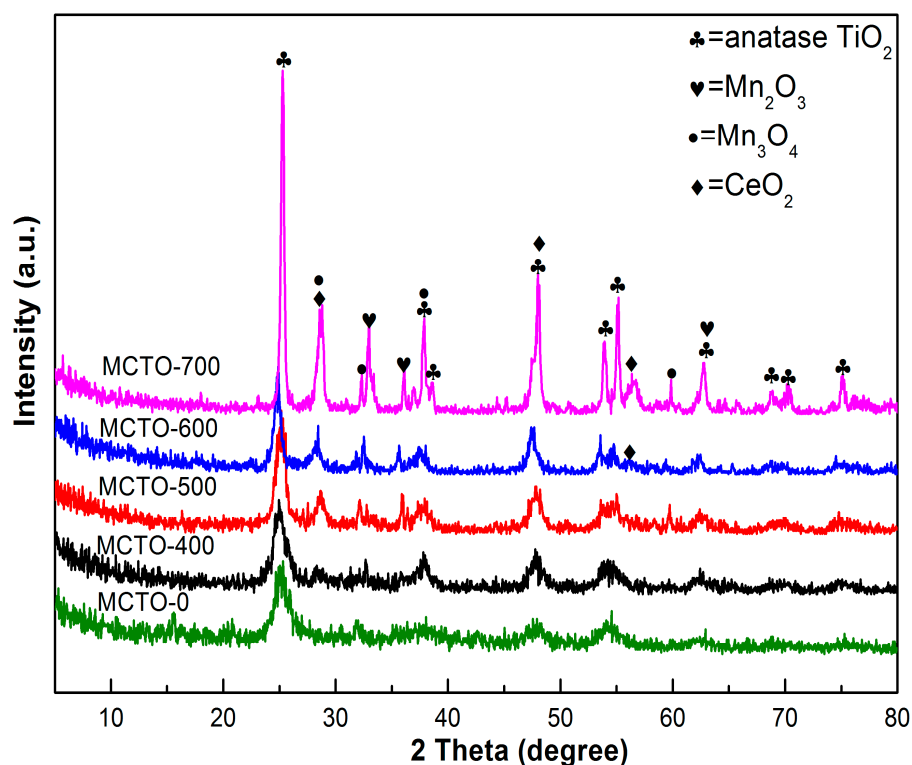
**Figure 2.** XRD patterns of MCTO-0, MCTO-400, MCTO-500, MCTO-600, and MCTO-700 catalysts.

**Table 1.** The mean crystallite sizes of metal oxides of different catalysts.

| Sample | $D_{TiO_2}$ (nm) | $D_{CeO_2}$ (nm) | $D_{Mn_2O_3}$ (nm) | $D_{Mn_3O_4}$ (nm) |
|--------|------------------|------------------|--------------------|--------------------|
| MCTO-0 | 7.8 | - | - | - |
| MCTO-400 | 9.4 | - | 6.8 | 15.3 |
| MCTO-500 | 11.5 | - | 12.5 | 20.8 |
| MCTO-600 | 16.2 | 8.0 | 13.0 | 21.5 |
| MCTO-700 | 21.5 | 13.6 | 17.8 | 38.8 |
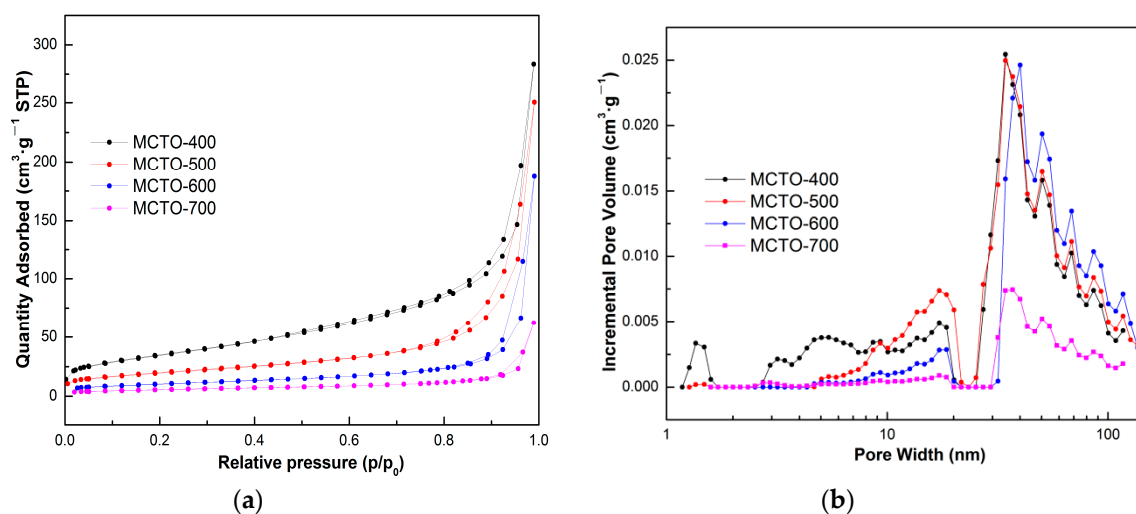


**Figure 3.** $N_2$ adsorption/desorption isotherms (**a**) and the corresponding pore size distributions (**b**) of MCTO-400, MCTO-500, MCTO-600, and MCTO-700.

It can be seen from the Table 2, the BET and pore volume of the catalysts decreased gradually with increasing the calcination temperature. And it is noted that the BET surface area of the MCTO-600

was not the highest among the catalysts, indicating that the specific surface area may not play an important role on the $NH_3$–SCR activity of MCTO-x catalysts [12]. Furthermore, the mean pore size of the MCTO-600 was largest among the catalysts due to the reduction of smaller pores below 20 nm while retaining larger pores above 20 nm.

**Table 2.** Brunauer–Emmett–Teller (BET) specific surface area and pore textures of the samples.

| Catalyst | Surface Area ($m^2 \cdot g^{-1}$) | Mean Pore Diameter (nm) | Pore Volume ($cm^3 \cdot g^{-1}$) |
|---|---|---|---|
| MCTO-400 | 127.1 | 14 | 0.44 |
| MCTO-500 | 71.6 | 22 | 0.38 |
| MCTO-600 | 35.8 | 32 | 0.29 |
| MCTO-700 | 18.9 | 20 | 0.095 |

Figure 4 shows the SEM images of Mn–Ce–Ti–O composite aerogels obtained at different calcination temperatures. It can be seen that the samples were composed by interconnected particles with a porous structure, and the particle size grew gradually with the increase of calcination temperature, showing an obvious particle agglomeration for the sample MCTO-700, in accordance with the above XRD and $N_2$ adsorption–desorption results.
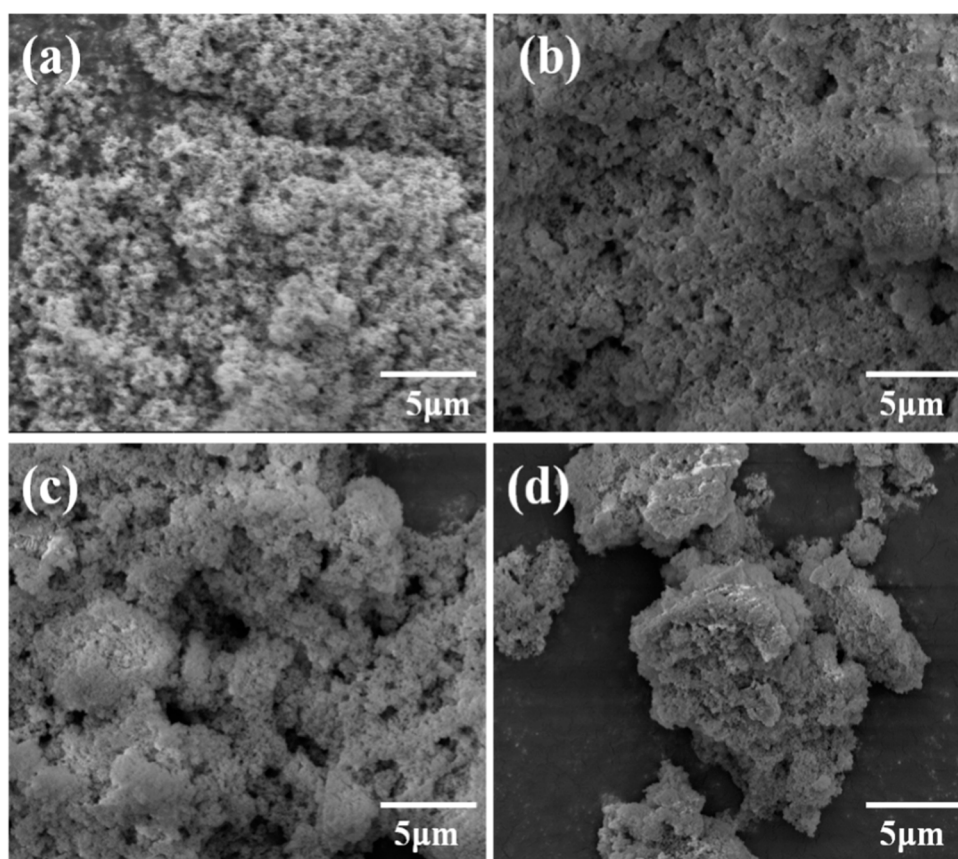


**Figure 4.** SEM images of MCTO-400 (**a**), MCTO-500 (**b**), MCTO-600 (**c**), and MCTO-700 (**d**).

XPS technology was used to study the surface atomic content and chemical states of Mn, Ce, Ti, and O. As shown in Figure 5a, the Mn 2p spectra contained two main peaks at 653.5–653.8 eV and 641.5–641.7 eV, which could be attributed to Mn 2p1/2 and Mn 2p3/2, respectively. The deconvolution of Mn 2p1/2 peak could obtain three peaks assigned to $Mn^{2+}$ (652.4 ± 0.2 eV), $Mn^{3+}$ (653.8 ± 0.3 eV), and $Mn^{4+}$ (654.9 eV ± 0.4), The Mn 2p3/2 could also be divided into three peaks ascribed to $Mn^{2+}$ (641.1 ± 0.2 eV), $Mn^{3+}$ (642.6 ± 0.3 eV), and $Mn^{4+}$ (644.1 ± 0.4 eV) [20,21]. The XPS spectra of Ce 3d in

Figure 5b could be divided into eight characteristic peaks, which were labeled as u (900.8–902.0 eV), u′ (903.3–904.0 eV), u″ (906.8–908.0 eV), u‴ (916.0–917.0 eV), v (882.0–882.4 eV), v′ (884.3–885.0 eV), v″ (887.9–888.4 eV), and v‴ (898.0–898.4 eV), The two peaks, u′ and v′, were attributed to $Ce^{3+}$ species, whereas another six peaks belonged to $Ce^{4+}$ species [14,38]. Two peaks, at ~464.5 eV and ~458.7 eV, were observed for the XPS spectra of Ti 2p, as shown in Figure 5c, which were attributed to Ti 2p3/2 and Ti 2p1/2, respectively, representing the characteristic $Ti^{4+}$ species [11,14]. The XPS spectra of O1s in Figure 5d exhibited two doublet peaks at 531.1–531.8 eV and 529.3–529.8 eV, which were assigned to the surface chemisorbed oxygen (denoted as $O_\alpha$) such as defect-oxide ($O_2^{2-}$ or $O^-$) and hydroxyl groups, and the lattice oxygen $O^{2-}$ (denoted as $O_\beta$), respectively [11,41]. The relative contents of different valence states could be calculated from the ratios of peak areas of XPS spectra, as listed in Table 3.
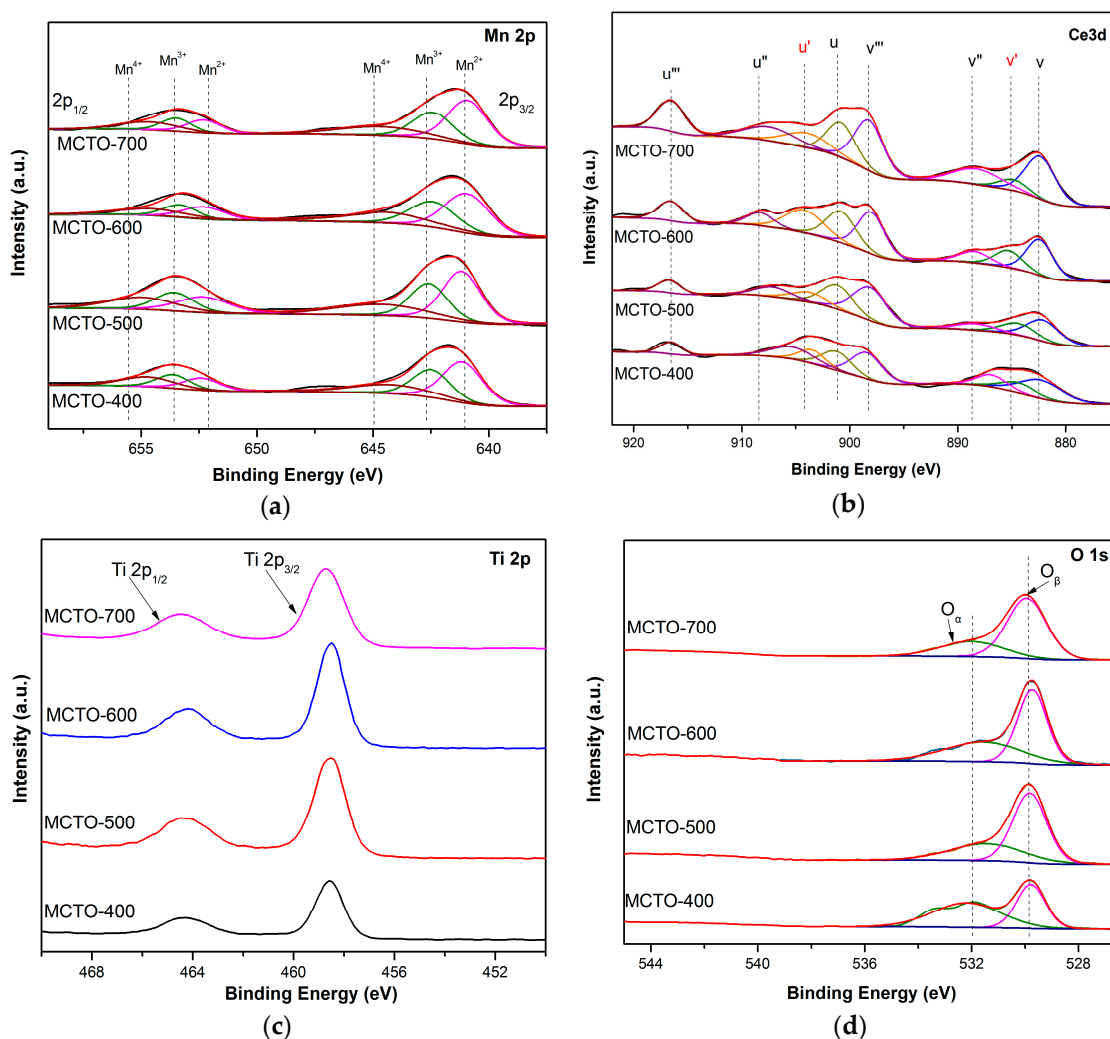


**Figure 5.** XPS spectra of the MCTO-400, MCTO-500, MCTO-600, and MCTO-700 catalysts: (**a**) Mn 2p, (**b**) Ce 3d, (**c**) Ti 2p, and (**d**) O 1s.

**Table 3.** Surface atomic compositions of catalysts measured by XPS.

| Sample | Atomic Composition (%) | | | | | $O_\alpha/(O_\alpha + O_\beta)$ (%) | $Ce^{3+}/Ce$ (%) | $Mn^{4+}/Mn$ (%) | $Mn^{3+}/Mn$ (%) | $Mn^{2+}/Mn$ (%) |
|---|---|---|---|---|---|---|---|---|---|---|
| | Mn | Ce | Ti | C | O | | | | | |
| MCTO-400 | 5.4 | 1.8 | 16.4 | 13.3 | 63.2 | 57.2 | 17.5 | 25.9 | 31.3 | 42.8 |
| MCTO-500 | 5.5 | 1.3 | 23.1 | 6.6 | 63.5 | 34.9 | 17.9 | 27.9 | 30.6 | 41.5 |
| MCTO-600 | 4.6 | 1.7 | 25.3 | 5.1 | 63.2 | 41.3 | 24.0 | 29.3 | 29.9 | 40.8 |
| MCTO-700 | 4.9 | 2.4 | 24.9 | 2.3 | 65.6 | 29.0 | 13.8 | 24.3 | 30.5 | 45.3 |

As can be seen from Table 3, with the increase of the calcination temperature, the relative atomic ratios of $Mn^{4+}/Mn$ on the surface of MCTO-x catalyst increased firstly and then decreased, and the highest ratio of $Mn^{4+}/Mn$ was present on the surface of the MCTO-600, which showed that an appropriate calcination temperature was favorable for the formation of $Mn^{4+}$. As the contents of the surface Mn element for the four samples were different, the absolute surface $Mn^{4+}$ contents for the MCTO-400, MCTO-500, MCTO-600, and MCTO-700 were 1.40%, 1.53%, 1.35%, and 1.19%, respectively. This difference could be caused by sintering and motion of primary nanoparticles in calcination, which caused different accessibilities for X-rays for different samples. It has been proved that $Mn^{4+}$ species and their redox cycle can accelerate the conversion of NO to $NO_2$, thereby enhancing the low-temperature $NH_3$–SCR performance via the "fast-SCR" path ($2NH_3 + NO + NO_2 = 2N_2 + 3H_2O$) [18], which displays a reaction rate 10 times higher than that of the standard SCR process [42]. The proportion of $Ce^{3+}/Ce$ and absolute $Ce^{3+}$ content on the surface of the MCTO-600 reached 24.0% and 0.41%, respectively, which were the highest among the four catalysts investigated. $Ce^{3+}$ could generate a charge imbalance to form oxygen vacancies and unsaturated chemical bonds on the surface of the catalysts and promote the migration of oxygen from the bulk to the surface, thus accelerating the oxidation of NO to $NO_2$ to facilitate the SCR reaction [22,23]. It has been widely reported that $O_\alpha$ species are more active than $O_\beta$ species due to their higher mobility, and a high $O_\alpha/(O_\alpha + O_\beta)$ ratio favors the oxidation of NO to $NO_2$ in $NH_3$–SCR to enhance the low-temperature activity of the catalyst [18,43]. It is noted that the percentage of $O_\alpha$ species was the highest for the MCTO-400 among the catalysts, which may be due to the smallest crystallite sizes at the lowest calcination temperature. The highest ratio of $O_\alpha/(O_\alpha + O_\beta)$ on the surface of the MCTO-400 catalyst corresponded to the most abundant Brønsted acid sites from the $NH_3$–TPD results. However, the MCTO-400 had the lowest $NH_3$–SCR performance among the four catalysts investigated. In addition, when the calcination temperature reached 700 °C, $O_\alpha$ decreased sharply, which may be due to the growth of crystallite size. These suggest that the number of surface chemisorbed oxygen might not the determining fact for the $NH_3$–SCR activity in this work.

The $H_2$–TPR technique was used to explore the reduction performance of the MCTO-x catalyst, and the obtained $H_2$–TPR profiles and corresponding $H_2$ consumption are shown in Figure 6a,b. The peak at 200–300 °C (denoted as peak "I") was assigned to $MnO_2 \rightarrow Mn_2O_3$ for the MCTO-600 and MCTO-700. The peak at 300–500 °C (denoted as peak "II") corresponded to $Mn_2O_3 \rightarrow Mn_3O_4$ for all samples. For the MCTO-400 and MCTO-500, the reduction at 200–300 °C corresponding to $MnO_2 \rightarrow Mn_2O_3$ was not well resolved with no apparent peak found. This could be caused by a smaller number of the high valence $Mn^{4+}$ at a lower calcination temperature. The peak at 500–600 °C (denoted as peak "III") was attributed to the reduction of $CeO_2$ to $Ce_2O_3$ or surface Mn–O–Ce species [22]. As shown in Figure 6b, as the calcination temperature increased, the total $H_2$ consumption of the catalysts increased firstly and then decreased. The MCTO-600 had the best reducibility, but its absolute surface $Mn^{4+}$ content was not the highest, which might be due to the fact that the accessibility of the X-ray for the surface of samples by XPS was different from that of the reactants, and that the former had a higher accessibility than the latter. With increases in the calcination temperature, the number of the high valence ions can increased, and therefore the total $H_2$ consumption can increase. The decrease of the total $H_2$ consumption beyond 600 °C can be caused by the growth of crystallite size due to

sintering and the decrease of the number of available reducible species. As the total $H_2$ consumption of the MCTO-600 exhibited the largest of 1.80 mmol $g^{-1}$, therefore, its low-temperature $NH_3$–SCR activity was the highest among the four samples, indicating that the reducibility of active species favored the improvement of the $NH_3$–SCR activity [14,18,38].
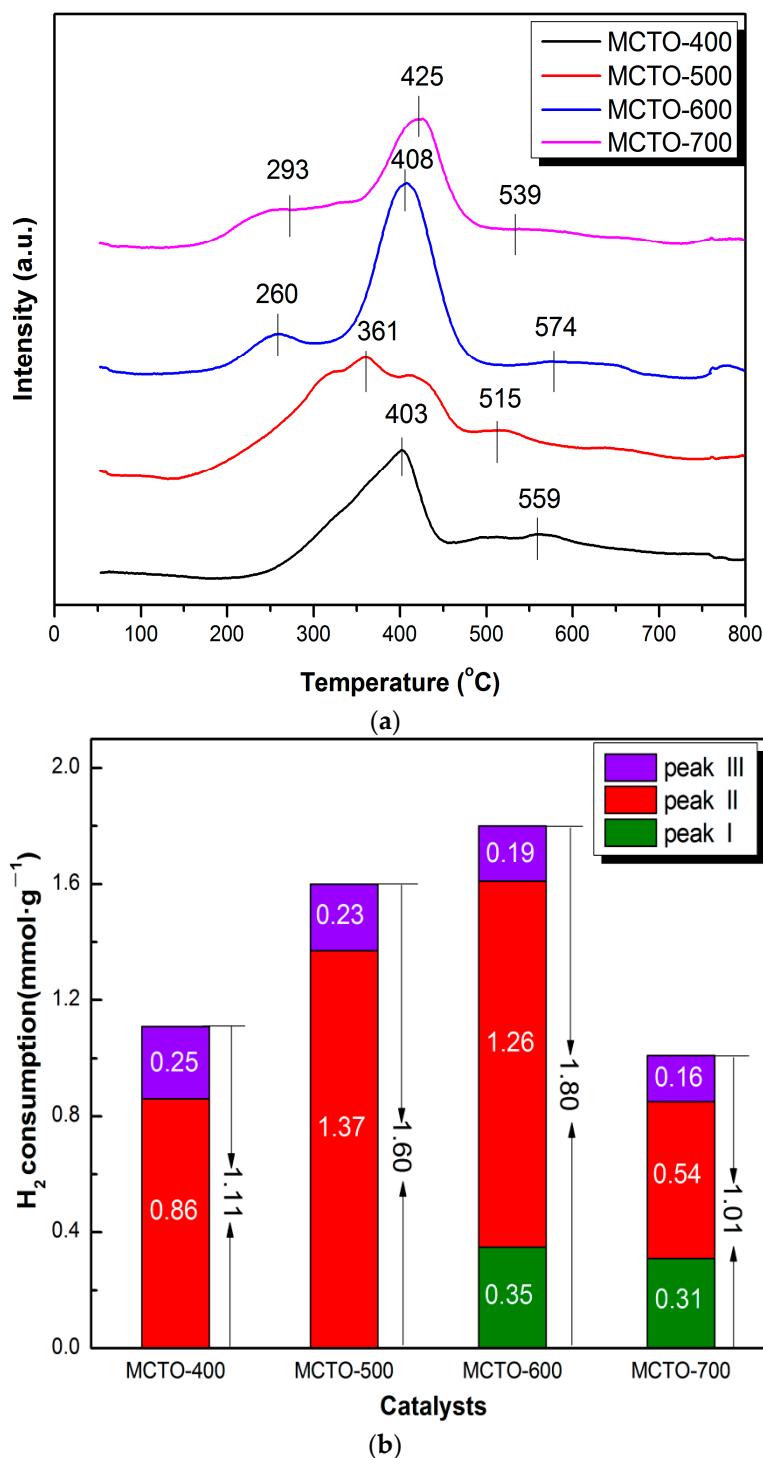


**Figure 6.** $H_2$–temperature programmed reduction (TPR) profiles (**a**) and the corresponding $H_2$ consumption (**b**) of the MCTO-400, MCTO-500, MCTO-600, and MCTO-700 catalysts.

It has been generally confirmed that the adsorption and activation of $NH_3$ on the acid sites of the catalyst surface is a key step in the $NH_3$–SCR, so the $NH_3$–TPD test was used to study the number

and the strength distribution of acid sites over the catalysts. As shown in Figure 7a, two evident peaks could be observed from the TPD profiles, namely peak "I" at 70–450 °C, ascribed to the $NH_3$ desorption by weak and medium acid sites, and peak "II" at 450–800 °C, due to the desorption of $NH_3$ at strong acidic sites. It was reported that the $NH_3$ molecules coordinated on the Lewis acid sites show a stronger thermal stability than the $NH_4^+$ ions formed on the Brønsted acid sites [44]. Thus, it can be inferred that the peak "I" belonged to the desorption of $NH_3$ on the Brønsted acid sites, and the peak "II" was attributed to the desorption of $NH_3$ from the Lewis acid sites. It can be seen from Figure 7b that the amount of the surface Brønsted acid sites of MCTO-x gradually decreased with the increase of calcination temperature, and the order was as follows: MCTO-400 (0.45 mmol·g$^{-1}$) > MCTO-500 (0.29 mmol·g$^{-1}$) > MCTO-600 (0.15 mmol·g$^{-1}$) > MCTO-700 (0.14 mmol·g$^{-1}$). With increases in the calcination temperature, the MCTO-600 exhibited the highest amount of adsorbed $NH_3$ on Lewis acid sites (0.46 mmol·g$^{-1}$), which had a stronger ability to adsorb and activate $NH_3$ than Brønsted acid sites to facilitate the $NH_3$–SCR process [2,45]. However, when the calcination temperature reached 700 °C, the amount of Lewis acid sites on the catalyst surface also began to decrease, which indicated that the higher calcination temperature led to the reduction of both the Brønsted and Lewis acid sites, causing weak $NH_3$ adsorption and activation. This might have been caused by the growth of crystallite size due to sintering and the decrease of the number of both the Brönsted and Lewis acid sites. The Brønsted acid sites were contributed to by –OH groups linked to Mn and Ce ions with different valences [46], which was why the amount of the surface Brønsted acid sites decreased with increases in the calcination temperature due to enhanced dehydration at high temperature. As $MnO_2$ was in an amorphous state as indicated by XRD, the Brønsted acid sites were contributed to by $Mn^{4+}$. The Lewis acid sites were mainly contributed to by the oxides of $Mn^{3+}$, $Mn^{2+}$, and $Ce^{3+}$ in a dehydrated state [47]. As $Mn_2O_3$ and $Mn_3O_4$ were in crystalline states while $Ce_2O_3$ was in an amorphous state as indicated in XRD, the Lewis acid sites were mainly contributed to by $Ce^{3+}$. The MCTO-600 had the highest amount of $Ce^{3+}$, so it had the most abundant Lewis acid sites.
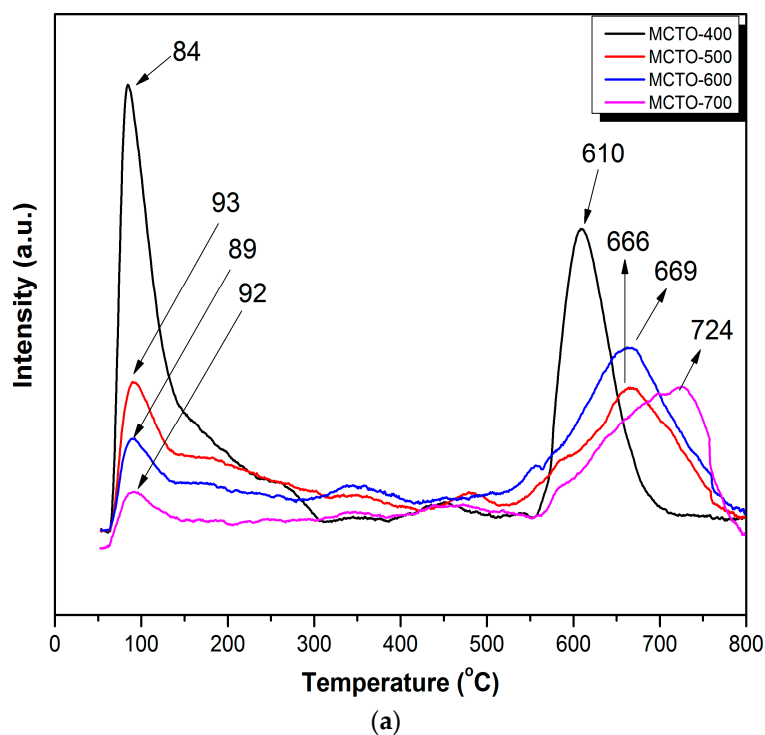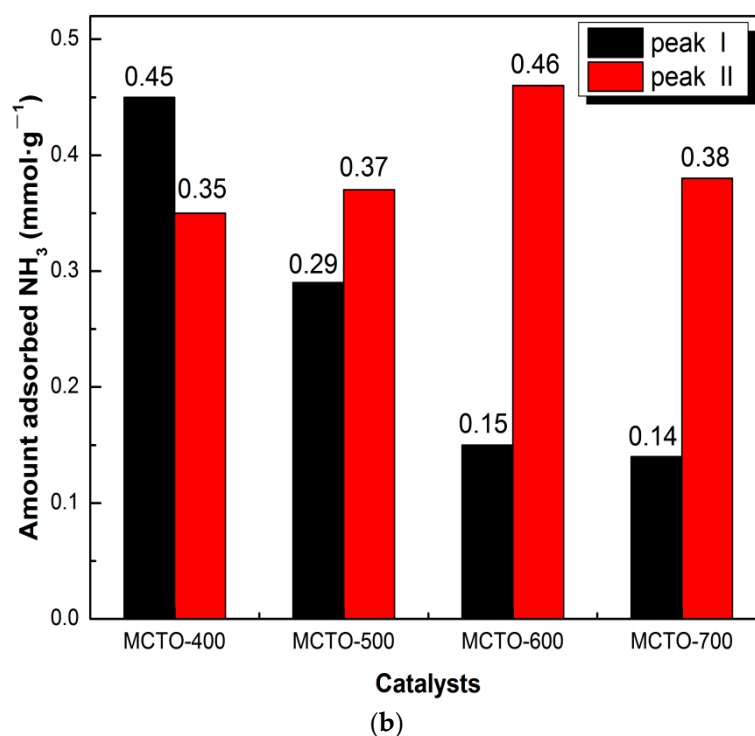


(a)

**Figure 7.** *Cont.*

**Figure 7.** $NH_3$–TPD profiles (**a**) and the corresponding amount of adsorbed $NH_3$ (**b**) of the MCTO-400, MCTO-500, MCTO-600, and MCTO-700 catalysts.

The in-situ DRIFTS was examined for the sample MCTO-600 in order to study the catalytic reaction mechanism of the Mn–Ce–Ti–O composite aerogel. During the experiment, $NH_3$ was firstly pre-adsorbed at 200 °C for 30 min, then purged with He for 30 min, and finally NO + $O_2$ was passed in for different times to obtain the results, as shown in Figure 8a. After the introduction of $NH_3$, some $NH_3$ species appeared on the surface of the MCTO-600 catalyst, including the coordinated $NH_3$ on the Lewis acid sites (1172, 1594, 3267, 3391 $cm^{-1}$) [48,49], the $NH_4^+$ adsorbed on Brønsted acid sites (1405 $cm^{-1}$), and $-NH_2$ (1540 $cm^{-1}$) [48,50]. From the different intensities of the Lewis and Brønsted acid species, it was found that Lewis acid sites were dominant in the MCTO-600, in accordance with the $NH_3$–TPD results. When NO + $O_2$ was introduced, the peak intensity of $NH_3$ (L) species on the catalyst surface gradually decreased and disappeared after 20 min. The bands of $NH_3$ (B) species showed no significant change in strength after 60 min of NO + $O_2$ introduction, indicating that it was Lewis, not Brønsted, acidity that contributed mainly to the $NH_3$–SCR reaction under this condition; so the largest amount of Lewis acid sites on the surface of the MCTO-600 catalyst played an important role for its highest $NH_3$–SCR activity. The peaks ascribed to the adsorbed NO appeared after 20 min, while the peaks attributed to $NH_3$ (L) species disappeared. The $-NH_2$ species, which may be the amides produced by the dehydrogenation of adsorbed $NH_3$, completely disappeared within 2 min, because they could react directly with gaseous NO to form the intermediate state $NH_2NO$, and finally rapidly decomposed into $N_2$ and $H_2O$ [2,19]. This suggests that adsorbed $NH_3$ (L) species reacted with gaseous NO and $O_2$, indicating that the Eley–Rideal (E–R) mechanism [2] was involved in the $NH_3$–SCR process. After introduction of NO + $O_2$ for 30 min, the surface of the catalyst was covered by adsorbed $NO_x$ species, including bridging nitrate species (1251 $cm^{-1}$) [11], monodentate nitrate species (1520 $cm^{-1}$) [51], bidentate nitrate species (1558 $cm^{-1}$) [15], and gaseous $NO_2$ species (1604 $cm^{-1}$) [48]. This suggests that the Langmuir–Hinshelwood (L–H) mechanism was also possible.
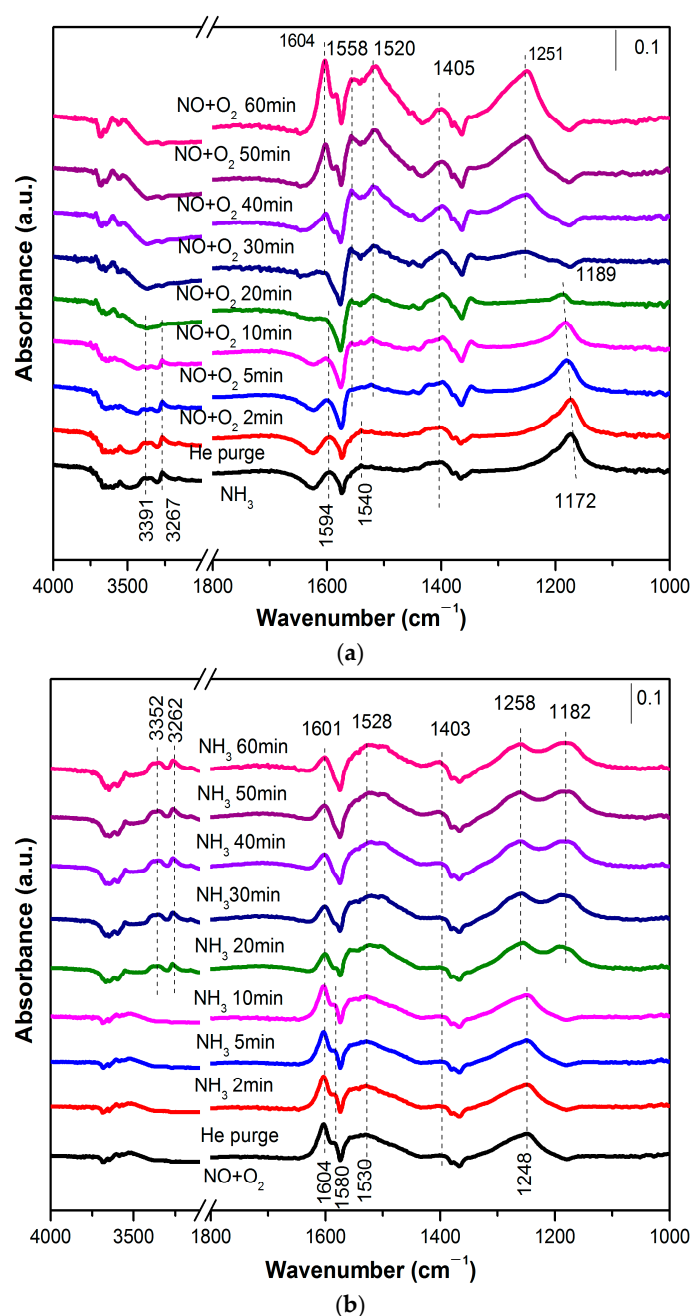
**Figure 8.** In-situ diffuse reflectance infrared Fourier transform spectra (DRIFTS) of NO + $O_2$ reacted with pre-adsorbed $NH_3$ species over MCTO-600 (**a**). In-situ DRIFTS of $NH_3$ reacted with pre-adsorbed NO + $O_2$ over MCTO-600 (**b**). Reaction conditions: T = 200 °C, 500 ppm of NO (when used), 500 ppm of $NH_3$ (when used), 5 vol. % of $O_2$ (when used), balance $N_2$.

Similarly, the transient SCR reaction of $NH_3$ with pre-adsorbed NO + $O_2$ on the MCTO-600 catalyst was recorded by in-situ DRIFTS, and the results of the reaction at different times are shown in Figure 8b. After the MCTO-600 catalyst was pretreated by NO + $O_2$, bridged nitrate species (1248 cm$^{-1}$), monodentate nitrate species (1403 and 1530 cm$^{-1}$), bidentate nitrate species (1580 cm$^{-1}$), and gaseous $NO_2$ (1604 cm$^{-1}$) species appeared on the catalyst surface. The co-existence of $NH_3$-adsorbed peaks (coordinated $NH_3$–L species at 1182, 3262, and 3352 cm$^{-1}$) and NO-adsorbed peaks (1403, 1528, and 1601 cm$^{-1}$) was found after $NH_3$ was introduced for 10 min, indicating that the Langmuir–Hinshelwood (L–H) mechanism was also involved in the $NH_3$–SCR process [2]. When $NH_3$ was introduced for less than 10 min, no peaks ascribed to adsorbed $NH_3$ were found. This could be

accounted for by the fact that the Lewis acid sites were abundant, which diluted the $NH_3$–adsorbed species, and that fast reaction between the adsorbed $NH_3$ and adsorbed NO occurred, leading to a low concentration of $NH_3$–adsorbed species that were out of the limits of DRIFTS. This implies that the Langmuir–Hinshelwood (L–H) mechanism was involved in the $NH_3$–SCR process as the activation energy for the Langmuir–Hinshelwood (L–H) mechanism was lower than that of the Eley–Rideal (E–R) mechanism [52].

In addition, a new band at 1258 $cm^{-1}$ may belong to the surface ammonium nitrate, which originated from the dimerization of $NO_2$ and the continuous reaction with $NH_3$ and $H_2O$ [19,53]. It has been confirmed that $NH_4NO_3$ is also an important intermediate component in the $NH_3$-SCR process, along the following reaction route: $NH_4NO_3 + NO \rightarrow NH_4NO_2 + NO_2$, $NH_4NO_2 \rightarrow N_2 + 2H_2O$ [54]. The presence of $NO_2$ species demonstrated that a high ratio of $Mn^{4+}/Mn$ facilitated the oxidation of NO to $NO_2$.

### 3.2. Catalytic Performance

The $NH_3$–SCR performance of Mn–Ce–Ti–O composite aerogels with different calcination temperatures is shown in Figure 9a. Almost no catalytic activity was observed for the uncalcined composite aerogel in the temperature range of 80–320 °C, showing only about 10% of NO conversion. However, the calcined products exhibited excellent low-temperature catalytic activity, and it was shown that the NO conversion increased with increases in the calcination temperature up to 600 °C and then decreases with further increases in the calcination temperature. The MCTO-600 exhibited the most excellent catalytic activity, achieving more than 80% of NO conversion at 160–320 °C and nearly 100% from 200–300 °C. Figure 9b shows the outlet $N_2O$ concentration and $N_2$ selectivity on the MCTO-600 catalyst. One hundred percent of $N_2$ selectivity was observed in the temperature range of 120–220 °C, whereas $N_2O$ was detected when the reaction temperature was above 220 °C, which may be because a part of $NH_3$ was oxidized at high temperatures [26]; nevertheless, more than 90% of $N_2$ selectivity was obtained at 240–320 °C.
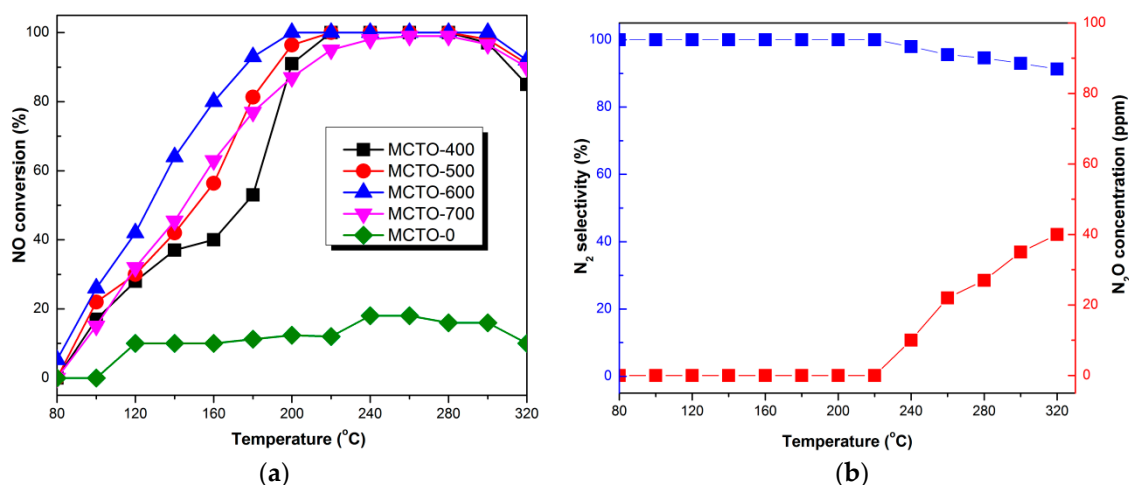


**Figure 9.** $NH_3$–selective catalytic reduction (SCR) activity of MCTO-0, MCTO-400, MCTO-500, MCTO-600, and MCTO-700 catalysts (**a**). $N_2$ selectivity of MCTO-600 (**b**). Reaction conditions: 500 ppm of NO, 500 ppm of $NH_3$, 5 vol. % of $O_2$, balance $N_2$, gas hourly space velocity (GHSV) = 14,400 $h^{-1}$.

### 3.3. Kinetics Parameters

As shown in Figure 10a–c, the calcination temperature had a certain influence on the reaction rate constant and $E_a$ of the obtained catalysts. With increases in temperature, the reaction rate constant increased gradually (Figure 10b), reaching the highest for the MCTO-600 at each temperature (18.16 $cm^3 \cdot s^{-1} \cdot g^{-1}$ at 160 °C, 26.90 $cm^3 \cdot s^{-1} \cdot g^{-1}$ at 180 °C, 43.55 $cm^3 \cdot s^{-1} \cdot g^{-1}$ at 200 °C, 57.54 $cm^3 \cdot s^{-1} \cdot g^{-1}$

at 220 °C, and 82.34 $cm^3 \cdot s^{-1} \cdot g^{-1}$ at 240 °C). Furthermore, as the calcination temperature increased, the $E_a$ of the catalyst decreased firstly and then increased as follows: MCTO-600 (35.75 $kJ \cdot mol^{-1}$) < MCTO-700 (45.36 $kJ \cdot mol^{-1}$) < MCTO-500 (50.71 $kJ \cdot mol^{-1}$) < MCTO-400 (51.41 $kJ \cdot mol^{-1}$) (Figure 10c), indicating the energy barrier of the $NH_3$–SCR reactions on the MCTO-600 was the lowest, which was related to its best $NH_3$–SCR performance. In addition, it should be mentioned that the $E_a$ of Mn–Ce–Ti–O composite catalysts prepared by this work were relatively lower compared with the other reported catalysts, such as the commercial V-W/Ti catalyst (73.9 $kJ \cdot mol^{-1}$) [10], Fe–ZSM-5 (54 $kJ \cdot mol^{-1}$) [5], and $WO_3/Fe_2O_3$ (62–66 $kJ \cdot mol^{-1}$) [37].



**(a)**



**(b)**

**(c)**
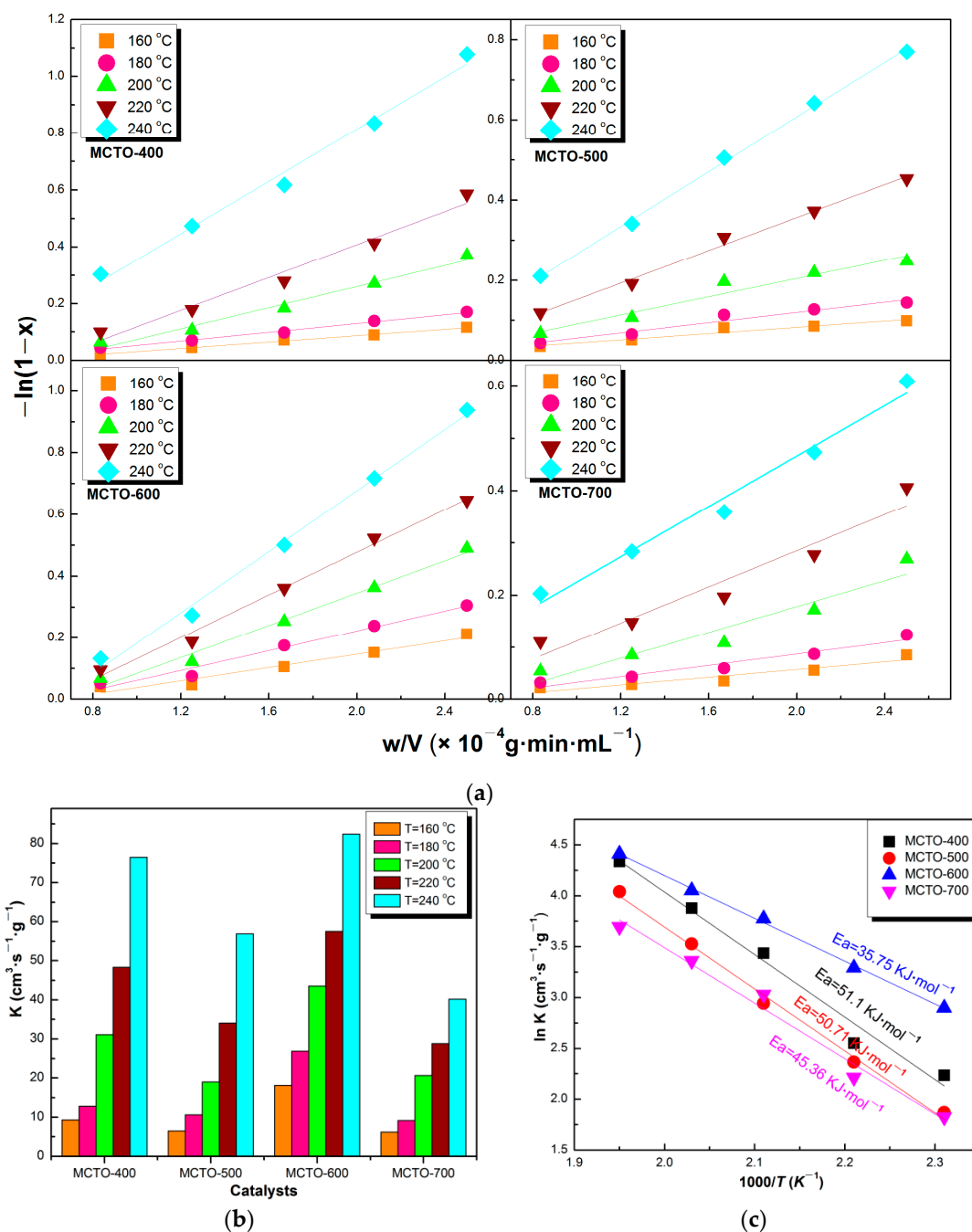
**Figure 10.** $-\ln(1 - x)$ versus w/V plots (**a**), reaction rate constant (**b**), and Arrhenius plots (**c**) of MCTO-400, MCTO-500, MCTO-600, and MCTO-700.

TOF was used to further compare the intrinsic activity of the catalysts at 160, 180, 200, and 220 °C, respectively, which was calculated based on the atomic percentage of Mn (the main active site) on the surface. As shown in Figure 11a,b, it can be seen that MCTO-600 presented the highest TOF value compared with that of MCTO-400, MCTO-500, and MCTO-700, which was $12.64 \times 10^{-5} \cdot s^{-1}$ at 160 °C, $15.83 \times 10^{-5} \cdot s^{-1}$ at 180 °C, $19.51 \times 10^{-5} \cdot s^{-1}$ at 200 °C, and $35.57 \times 10^{-5} \cdot s^{-1}$ at 220 °C, further demonstrating that NO conversion on the MCTO-600 was highest, in accordance with the results from the activation energy.



(**a**)   (**b**)
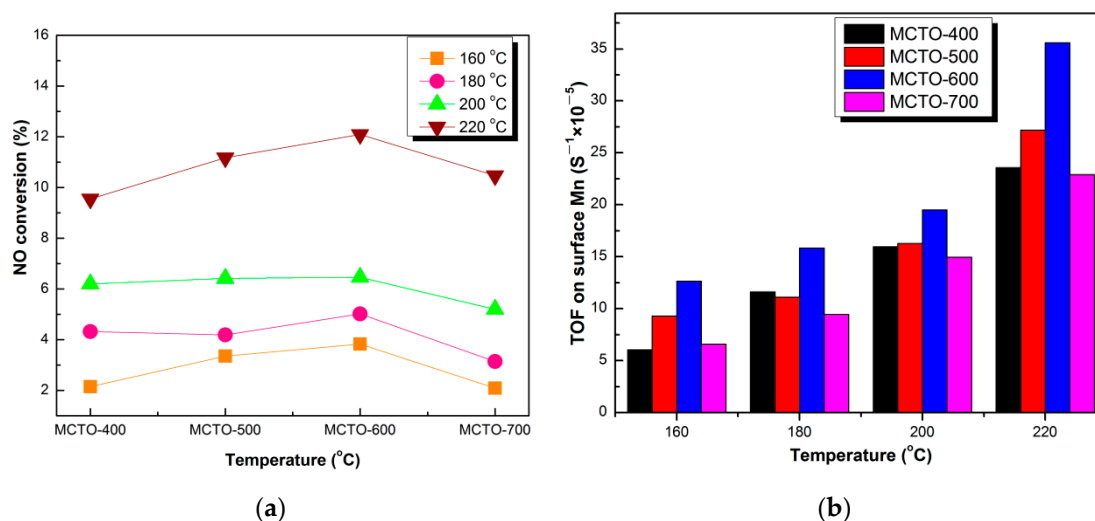
**Figure 11.** $NH_3$–SCR performance (**a**) and the corresponding TOF (**b**) of MCTO-400, MCTO-500, MCTO-600, and MCTO-700 at different temperatures. Reaction conditions: 500 ppm of NO, 500 ppm of $NH_3$, 5 vol. % $O_2$, balance $N_2$, catalyst mass = 20 mg, flow rate = 240 mL·min$^{-1}$, GHSV ≈ 200,000 h$^{-1}$.

*3.4. Influence of $SO_2$ and $H_2O$ and Stability Test*

In actual industrial processes, some residual $SO_2$ is present in the desulfurized flue gas, which may poison and deactivate the denitration catalysts at low temperature. Therefore, the $SO_2$ tolerance performance of the MCTO-600 catalyst was further studied, as shown in Figure 12a. The NO removal efficiency was stabilized at 100% for approximately 2 h at 200 °C prior to the injection of $SO_2$. When 100 ppm of $SO_2$ was introduced into the simulated flue gas, the NO conversion of the catalyst remained nearly 100% within 6 h, which was unchanged for the next 2 h after the injection of $SO_2$ was cut off, indicating the excellent $SO_2$ resistance for the MCTO-600. It has been acknowledged that the $TiO_2$ and $CeO_2$ components can improve the $SO_2$ tolerance of Mn-based catalysts, because $TiO_2$ can restrain the $SO_2$ adsorption due to the weak interaction between $SO_2$ and $TiO_2$, and $CeO_2$ can act as a sacrificial site to alleviate the sulfation of active $MnO_x$ [1,24,27,55]. However, the reported $SO_2$ resistant performance of $MnO_x$–$CeO_2$–$TiO_2$ catalysts was limited to some extent, as listed in Table 4. The excellent $SO_2$ tolerance of the MCTO-600 catalyst in this work can be attributed to its largest mesopore size with an average pore size of 32 nm compared with that of the other reported catalysts (6.7–17.3 nm), because the decomposition of ammonium sulfate occurs more easily in larger pores [29–31]. In addition, the above in-situ DRIFTS results showed that the $NH_3$–SCR reaction over the MCTO-600 catalyst followed both the E–R and L–H mechanisms, especially for the E–R pathway; namely, the gaseous NO could react directly with the active $NH_3$ species adsorbed on Lewis acid sites, which is also beneficial to the superior $SO_2$ resistance ability [25,56].
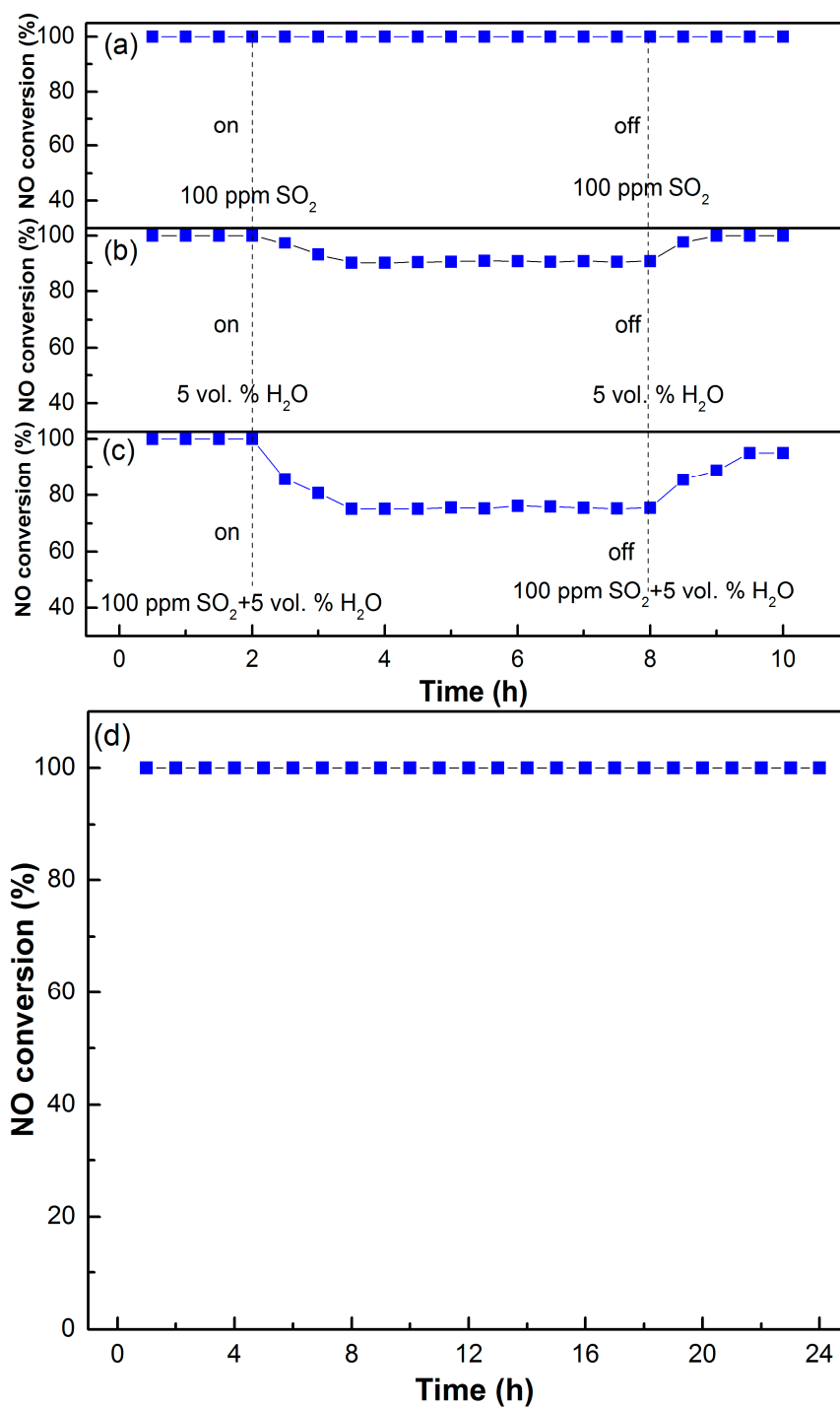
**Figure 12.** The influence of $SO_2$ (**a**), $H_2O$ (**b**), and $SO_2 + H_2O$ (**c**) on NO conversion and long-time stability test (**d**) of the MCTO-600 catalyst. Reaction conditions: T = 200 °C, 500 ppm of NO, 500 ppm of $NH_3$, 5 vol. % of $O_2$, 5 vol. % of $H_2O$ (when used), 100 ppm of $SO_2$ (when used), and balance $N_2$; GHSV = 14,400 $h^{-1}$.

**Table 4.** A comparison of anti-$SO_2$ performance of $MnO_x$–$CeO_2$–$TiO_2$ catalysts prepared by different methods in the reported literatures.

| Catalysts | Average Pore Size | Preparation Methods | Reaction Conditions | NO Conversion Before and After Introducing $SO_2$ | Refs |
|---|---|---|---|---|---|
| $MnO_x$–$CeO_2$@$TiO_2$ | 13.3 nm | three-step method | T = 180 °C, [NO] = [$NH_3$] = 500 ppm, [$O_2$] = 5%, [$SO_2$] = 200 ppm, GHSV = 24,000 $h^{-1}$ | decline from 100% to 70% | [26] |
| Mn–Ce/$TiO_2$ | 9.0 nm | co-precipitation method | T = 120 °C, [NO] = [$NH_3$] = 600 ppm, [$O_2$] = 3%, [$SO_2$] = 700 ppm, GHSV = 40,000 $h^{-1}$ | decline from 92.5% to 34.6% | [33] |
| Mn–Ce/$TiO_2$ | 6.7 nm | sol–gel method | T = 150 °C, [NO] = [$NH_3$] = 800 ppm, [$O_2$] = 3%, [$SO_2$] = 100 ppm, GHSV = 40,000 $h^{-1}$ | decline from 100% to 60% | [24] |
| $MnO_x$–$CeO_2$/$TiO_2$ | 13.7 nm | one-step hydrothermal method | T = 180 °C, [NO] = [$NH_3$] = 500 ppm, [$O_2$] = 5%, [$SO_2$] = 200 ppm, GHSV = 24,000 $h^{-1}$ | decline from 100% to 47% | [26] |
| $MnO_x$/$CeO_2$–$TiO_2$ | 17.3 nm | wet impregnation | T = 180 °C, [NO] = 200 ppm, [$NH_3$] = 220 ppm, [$O_2$] = 8%, [$SO_2$] = 100 ppm, GHSV = 60,000 $h^{-1}$ | decline from 84% to 62% | [32] |
| MnCe/TNTs | 13.6 nm | hydrothermal method | T = 150 °C, [NO] = 720 ppm, [$NH_3$] = 800 ppm, [$O_2$] = 3%, [$SO_2$] = 100 ppm, GHSV = 100,000 $h^{-1}$ | decline from 92% to 84% | [12] |
| Mn–Ce–Ti–O composite aerogels | 32.5 nm | one-pot sol–gel method | T = 200 °C, [NO] = [$NH_3$] = 500 ppm, [$O_2$] = 5%, [$SO_2$] = 100 ppm, GHSV = 14,400 $h^{-1}$ | maintaining at 100% | in this work |

Meanwhile, the $H_2O$ resistance of the MCTO-600 catalyst was also investigated, as shown in Figure 12b. When 5 vol. % of $H_2O$ vapor was introduced into the system, the NO conversion decreased from 100% to 90% in the first 2 h and remained stable for the next 4 h, which returned to 100% after the $H_2O$ vapor was cut off, which may have been due to the fact that the adsorption of $H_2O$ at the active sites was reversible, and the occupied active sites could be easily regenerated after $H_2O$ desorption [55,57]. When 100 ppm of $SO_2$ and 5 vol. % of $H_2O$ vapor were injected into the flue gas simultaneously, as shown in Figure 12c, the NO conversion of the MCTO-600 catalyst reduced from 100% to 75% within 2 h and remained stable for the next 4 h, which then gradually increased from 75% to 95% within 2.5 h after $SO_2$ + $H_2O$ was cut off, suggesting that the passivation of the catalyst by $SO_2$ + $H_2O$ included reversible and irreversible parts [58]. These results indicated that the coexistence of $SO_2$ and $H_2O$ vapor at a low temperature had a greater impact on the NO removal than that of $SO_2$ alone, which may have been due to the fact that $H_2O$ can accelerate the deposition of sulfates on the surface of catalyst, thereby intensifying the poisoning of $SO_2$ [59,60]. In addition, the stability and longevity of the catalyst are also important for practical applications, as shown in Figure 12d; the NO removal efficiency of the MCTO-600 catalyst was stabilized at 100% within 24 h under the test conditions, demonstrating its excellent long-term stability.

## 4. Conclusions

In this work, the Mn–Ce–Ti–O composite aerogel with a large mesopore size was successfully prepared via a one-pot sol-gel method by using propylene oxide as a network gel inducer and ethyl acetoacetate as a complexing agent, and which was used for $NH_3$–SCR of simulated flue gas. The results indicate that the Mn–Ce–Ti–O catalyst calcined at 600 °C exhibits the highest $NH_3$–SCR activity, good $N_2$ selectivity, lowest $E_a$, excellent $SO_2$ resistance, and long-term stability. Its highest $NH_3$–SCR activity is related to the most abundant Lewis acid sites and the best reducibility among the four catalysts calcinated at different temperatures (400, 500, 600, and 700 °C). The Lewis acid

sites are mainly contributed by $Ce^{3+}$ while the Brønsted acid sites mainly by $Mn^{4+}$. The Lewis acid sites play a more important role than the Brønsted acid sites do in our catalysts investigated. Its superior $SO_2$ resistance to the other reported $MnO_x$–$CeO_2$–$TiO_2$ catalysts can be mainly attributed to its large mesopore size with an average pore size of 32 nm. The abundant Lewis acid sites are another factor that alleviates sulfation of $NH_3$, which may reduce vapor pressure of $NH_3$ greatly. Both the Langmuir–Hinshelwood (L–H) mechanism and the Eley–Rideal (E–R) mechanism are involved in the $NH_3$–SCR. The results of this study may provide a good opportunity for preparing and designing $NH_3$–SCR catalysts with superior sulfur tolerance and low temperature activity.

**Conflicts of Interest:** The authors declare no conflict of interest.

## References

1.　Zhang, L.; Zhang, D.; Zhang, J.; Cai, S.; Fang, C.; Huang, L.; Li, H.; Gao, R.; Shi, L. Design of meso-TiO$_2$@MnOx–CeO$_x$/CNTs with a core-shell structure as DeNO$_x$ catalysts: Promotion of activity, stability and SO$_2$-tolerance. *Nanoscale* **2013**, *5*, 9821–9829. [CrossRef] [PubMed]

2.　Liu, J.; Li, X.; Zhao, Q.; Ke, J.; Xiao, H.; Lv, X.; Liu, S.; Tadé, M.; Wang, S. Mechanistic investigation of the enhanced NH$_3$-SCR on cobalt-decorated Ce–Ti mixed oxide: In situ FTIR analysis for structure-activity correlation. *Appl. Catal. B Environ.* **2017**, *200*, 297–308. [CrossRef]

3.　Xie, A.; Tang, Y.; Huang, X.; Jin, X.; Gu, P.; Luo, S.; Yao, C.; Li, X. Three-dimensional nanoflower MnCrO$_x$/Sepiolite catalyst with increased SO$_2$ resistance for NH$_3$–SCR at low temperature. *Chem. Eng. J.* **2019**, *370*, 897–905. [CrossRef]

4.　Shao, J.; Lin, F.; Li, Y.; Tang, H.; Wang, Z.; Liu, P.; Chen, G. Co-precipitation synthesized MnO$_x$–CeO$_2$ mixed oxides for NO oxidation and enhanced resistance to low concentration of SO$_2$ by metal addition. *Catalysts* **2019**, *9*, 519. [CrossRef]

5.　Huang, H.; Long, R.; Yang, R. Kinetics of selective catalytic reduction of NO with NH$_3$ on Fe–ZSM-5 catalyst. *Appl. Catal. A Gen.* **2002**, *235*, 241–251. [CrossRef]

6.　Yang, S.; Li, J.; Wang, C.; Chen, J.; Ma, L.; Chang, H.; Chen, L.; Peng, Y.; Yan, N. Fe–Ti spinel for the selective catalytic reduction of NO with NH$_3$: Mechanism and structure-activity relationship. *Appl. Catal. B Environ.* **2012**, *117–118*, 73–80. [CrossRef]

7.　Wei, B.; Yang, W.; Wang, J.; Tan, H.; Zhou, S.; Wang, F.; Ma, J. Study on reduction mechanism of Fe$_2$O$_3$ by NH$_3$ under SNCR condition. *Fuel* **2019**, *255*, 115814. [CrossRef]

8.　Xi, H.; Zhou, S.; Zhou, J. New experimental results of NO removal from simulated marine engine exhaust gases by Na$_2$S$_2$O$_8$/urea solutions. *Chem. Eng. J.* **2019**, *362*, 12–20. [CrossRef]

9.　Song, L.; Ma, K.; Tian, W.; Ji, J.; Liu, C.; Tang, S.; Jiang, W.; Yue, H.; Liang, B. An environmentally friendly FeTiSO$_x$ catalyst with a broad operation-temperature window for the NH$_3$-SCR of NO$_x$. *AIChE J.* **2019**, *65*, e16684. [CrossRef]

10.　Michalow-Mauke, K.; Lu, Y.; Kowalski, K.; Graule, T.; Nachtegaal, M.; Kröcher, O.; Ferri, D. Flame-Made WO$_3$/CeO$_x$–TiO$_2$ Catalysts for Selective Catalytic Reduction of NO$_x$ by NH$_3$. *ACS. Catal.* **2015**, *5*, 5657–5672. [CrossRef]

11.　Mu, J.; Li, X.; Sun, W.; Fan, S.; Wang, X.; Wang, L.; Qin, M.; Gan, G.; Yin, Z.; Zhang, D. Enhancement of Low-temperature catalytic activity over a highly dispersed Fe–Mn/Ti catalyst for selective catalytic reduction of NO$_x$ with NH$_3$. *Ind. Eng. Chem. Res.* **2018**, *57*, 10159–10169. [CrossRef]

12.　Chen, X.; Wang, P.; Fang, P.; Ren, T.; Liu, Y.; Cen, C.; Wang, H.; Wu, Z. Tuning the property of Mn–Ce composite oxides by titanate nanotubes to improve the activity, selectivity and SO$_2$/H$_2$O tolerance in middle temperature NH$_3$–SCR reaction. *Fuel Process. Technol.* **2017**, *167*, 221–228. [CrossRef]

13.  Gao, F.; Tang, X.; Yi, H.; Li, J.; Zhao, S.; Wang, J.; Chu, C.; Li, C. Promotional mechanisms of activity and SO$_2$ tolerance of Co-or Ni-doped MnO$_x$–CeO$_2$ catalysts for SCR of NO$_x$ with NH$_3$ at low temperature. *Chem. Eng. J.* **2017**, *317*, 20–31. [CrossRef]

14.  Leng, X.; Zhang, Z.; Li, Y.; Zhang, T.; Ma, S.; Yuan, F.; Niu, X.; Zhu, Y. Excellent low temperature NH$_3$–SCR activity over MnaCe$_{0.3}$TiO$_x$ (a = 0.1–0.3) oxides: Influence of Mn addition. *Fuel Process. Technol.* **2018**, *181*, 33–43. [CrossRef]

15.  Chen, L.; Yuan, F.; Li, Z.; Niu, X.; Zhu, Y. Synergistic effect between the redox property and acidity on enhancing the low temperature NH$_3$–SCR activity for NO$_x$ removal over the Co$_{0.2}$Ce$_x$Mn$_{0.8-}$xTi$_{10}$ (x = 0–0.40) oxides catalysts. *Chem. Eng. J.* **2018**, *354*, 393–406. [CrossRef]

16.  Ma, M.; Ma, X.; Cui, S.; Liu, T.; Tian, Y.; Wang, Y. Low Temperature NH$_3$–SCR over Mn–Ce Oxides Supported on MCM-41 from Diatomite. *Materials* **2019**, *12*, 3654. [CrossRef]

17.  Meng, D.; Zhan, W.; Guo, Y.; Guo, Y.; Wang, L.; Lu, G. A highly effective catalyst of Sm–MnO$_x$ for the NH$_3$–SCR of NO$_x$ at low temperature: Promotional role of Sm and its catalytic performance. *ACS. Catal.* **2015**, *5*, 5973–5983. [CrossRef]

18.  Wang, Z.; Guo, R.; Shi, X.; Liu, X.; Qin, H.; Liu, Y.; Duan, C.; Guo, D.; Pan, W. The superior performance of CoMnO$_x$ catalyst with ball-flowerlike structure for low-temperature selective catalytic reduction of NOx by NH$_3$. *Chem. Eng. J.* **2020**, *381*, 122753. [CrossRef]

19.  Liu, F.; Shan, W.; Lian, Z.; Xie, L.; Yang, W.; He, H. Novel MnWO$_x$ catalyst with remarkable performance for low temperature NH$_3$-SCR of NO$_x$. *Catal. Sci. Technol.* **2013**, *3*, 2699–2707. [CrossRef]

20.  Yang, S.; Wang, C.; Li, J.; Yan, N.; Ma, L.; Chang, H. Low temperature selective catalytic reduction of NO with NH$_3$ over Mn–Fe spinel: Performance, mechanism and kinetic study. *Appl. Catal. B Environ.* **2011**, *110*, 71–80. [CrossRef]

21.  Wang, F.; Xie, Z.; Liang, J.; Fang, B.; Piao, Y.; Hao, M.; Wang, Z. Tourmaline-modified FeMnTiO$_x$ catalysts for improved low temperature NH$_3$–SCR performance. *Environ. Sci. Technol.* **2019**, *53*, 6989–6996. [CrossRef] [PubMed]

22.  Ren, S.; Yang, J.; Zhang, T.; Jiang, L.; Long, H.; Guo, F.; Kong, M. Role of cerium in improving NO reduction with NH$_3$ over Mn–Ce/ASC catalyst in low-temperature flue gas. *Chem. Eng. Res. Des.* **2018**, *133*, 1–10. [CrossRef]

23.  Li, Q.; Li, X.; Li, W.; Zhong, L.; Zhang, C.; Fang, Q.; Chen, G. Effect of preferential exposure of anatase TiO2{001} facets on the performance of Mn–Ce/TiO$_2$ catalysts for low-temperature selective catalytic reduction of NO$_x$ with NH$_3$. *Chem. Eng. J.* **2019**, *369*, 26–34. [CrossRef]

24.  Jin, R.; Liu, Y.; Wang, Y.; Cen, W.; Wu, Z.; Wang, H.; Weng, X. The role of cerium in the improved SO$_2$ tolerance for NO reduction with NH$_3$ over Mn–Ce/TiO$_2$ catalyst at low temperature. *Appl. Catal. B Environ.* **2014**, *148–149*, 582–588. [CrossRef]

25.  Han, L.; Cai, S.; Gao, M.; Hasegawa, J.Y.; Wang, P.; Zhang, J.; Shi, L.; Zhang, D. Selective Catalytic Reduction of NOx with NH$_3$ by using novel catalysts: State of the art and future prospects. *Chem. Rev.* **2019**, *119*, 10916–10976. [CrossRef]

26.  Ma, D.; Yang, L.; Huang, B.; Wang, L.; Wang, X.; Sheng, Z.; Dong, F. MnOx–CeO$_2$@TiO$_2$ core-shell composites for low temperature SCR of NO$_x$. *New J. Chem.* **2019**, *43*, 15161–15168. [CrossRef]

27.  Chang, H.; Chen, X.; Li, J.; Ma, L.; Wang, C.; Liu, C.; Schwank, J.W.; Hao, J. Improvement of activity and SO$_2$ tolerance of Sn-Modified MnO$_x$–CeO$_2$ Catalysts for NH$_3$–SCR at Low Temperatures. *Environ. Sci. Technol.* **2013**, *47*, 5294–5301. [CrossRef]

28.  Yu, J.; Guo, F.; Wang, Y.; Zhu, J.; Liu, Y.; Su, F.; Gao, S.; Xu, G. Sulfur poisoning resistant mesoporous Mn-base catalyst for low-temperature SCR of NO with NH$_3$. *Appl. Catal. B Environ.* **2010**, *95*, 160–168. [CrossRef]

29.  Soh, B.W.; Nam, I.S. Effect of support morphology on the sulfur tolerance of V$_2$O$_5$/Al$_2$O$_3$ catalyst for the reduction of NO by NH$_3$. *Ind. Eng. Chem. Res.* **2003**, *42*, 2975–2986. [CrossRef]

30.  Guo, K.; Fao, G.; Gu, D.; Yu, S.; Ma, K.; Liu, A.; Tan, W.; Wang, J.; Du, X.; Zhou, W.; et al. Pore size expansion accelerates ammonium bisulfate decomposition for improved sulfur resistance in low-temperature NH$_3$–SCR. *ACS Appl. Mater. Interfaces.* **2019**, *11*, 4900–4907. [CrossRef]

31.  Ma, K.; Guo, K.; Li, L.; Zou, W.; Tang, C.; Dong, L. Cavity size dependent SO$_2$ resistance for NH$_3$–SCR of hollow structured CeO$_2$–TiO$_2$ catalysts. *Catal. Commun.* **2019**, *128*, 105719. [CrossRef]

32.  Lee, S.M.; Park, K.H.; Hong, S.C. MnO$_x$/CeO$_2$–TiO$_2$ mixed oxide catalysts for the selective catalytic reduction of NO with NH$_3$ at low temperature. *Chem. Eng. J.* **2012**, *195–196*, 323–331. [CrossRef]

33. Sheng, Z.; Hu, Y.; Xue, J.; Wang, X.; Liao, W. SO$_2$ poisoning and regeneration of Mn–Ce/TiO$_2$ catalyst for low temperature NO$_x$ reduction with NH$_3$. *J. Rare Earths* **2012**, *30*, 676–682. [CrossRef]

34. Peng, Y.; Li, K.; Li, J. Identification of the active sites on CeO$_2$–WO$_3$ catalysts for SCR of NOx with NH$_3$: An in-situ IR and Raman spectroscopy study. *Appl. Catal. B Environ.* **2013**, *140–141*, 483–492. [CrossRef]

35. Zhang, D.; Zhang, L.; Shi, L.; Fang, C.; Li, H.; Gao, R.; Huang, L.; Zhang, J. In situ supported MnO$_x$–CeO$_x$ on carbon nanotubes for the low-temperature selective catalytic reduction of NO with NH$_3$. *Nanoscale* **2013**, *5*, 1127–1136. [CrossRef]

36. Han, L.; Gao, M.; Hasegawa, J.; Li, S.; Shen, Y.; Li, H.; Shi, L.; Zhang, D. SO$_2$–tolerant selective catalytic reduction of NO$_x$ over Meso–TiO$_2$@Fe$_2$O$_3$@Al$_2$O$_3$ Metal-Based Monolith catalysts. *Environ. Sci. Technol.* **2019**, *53*, 6462–6473. [CrossRef]

37. Zhang, J.; Huang, Z.; Du, Y.; Wu, X.; She, H.; Jiang, G. Atomic-scale insights into the nature of active sites in Fe$_2$O$_3$-supported submonolayer WO$_3$ catalysts for selective catalytic reduction of NO with NH$_3$. *Chem. Eng. J.* **2020**, *381*, 122668. [CrossRef]

38. Jiang, L.; Liu, Q.; Ran, G.; Kong, M.; Ren, S.; Yang, J.; Li, J. V$_2$O$_5$–modified Mn–Ce/AC catalyst with high SO$_2$ tolerance for low temperature NH$_3$-SCR of NO. *Chem. Eng. J.* **2019**, *370*, 810–821. [CrossRef]

39. Xiao, X.; Sheng, Z.; Yang, L.; Dong, F. Low-temperature selective catalytic reduction of NOx with NH$_3$ over a manganese and cerium oxide/graphene composite prepared by a hydrothermal method. *Catal. Sci. Technol.* **2016**, *6*, 1507–1514. [CrossRef]

40. Ye, B.; Lee, M.; Jeong, B.; Kim, J.; Lee, D.H.; Baik, J.M.; Kim, H.D. Partially reduced graphene oxide as a support of Mn–Ce/TiO$_2$ catalyst for selective catalytic reduction of NO$_x$ with NH$_3$. *Catal. Today* **2019**, *328*, 300–306. [CrossRef]

41. Liu, F.; He, H.; Ding, Y.; Zhang, C. Effect of manganese substitution on the structure and activity of iron titanate catalyst for the selective catalytic reduction of NO with NH$_3$. *Appl. Catal. B Environ.* **2009**, *93*, 194–204. [CrossRef]

42. Koebel, M.; Elsener, M.; Madia, G. Reaction pathways in the selective catalytic reduction process with NO and NO$_2$ at low temperatures. *Ind. Eng. Chem. Res.* **2001**, *40*, 52–59. [CrossRef]

43. Li, W.; Zhang, C.; Li, X.; Tan, P.; Zhou, A.; Fang, Q.; Chen, G. Ho-modified Mn–Ce/TiO$_2$ for low-temperature SCR of NO$_x$ with NH$_3$: Evaluation and characterization. *Chin. J. Catal.* **2018**, *39*, 1653–1663. [CrossRef]

44. Zhang, L.; Shi, L.; Huang, L.; Zhang, J.; Gao, R.; Zhang, D. Rational design of high-performance DeNO$_x$ catalysts bsed on MnxCo$_{3-x}$O$_4$ nanocages derived from Metal-Organic Frameworks. *ACS Catal.* **2014**, *4*, 1753–1763. [CrossRef]

45. Li, C.; Tang, X.; Yi, H.; Wang, L.; Cui, X.; Chu, C.; Li, J.; Zhang, R.; Yu, Q. Rational design of template-free MnO$_x$–CeO$_2$ hollow nanotube as de-NO$_x$ catalyst at low temperature. *Appl. Surf. Sci.* **2018**, *428*, 924–932. [CrossRef]

46. Marbán, G.; Solís, T.V.; Fuertes, A.B. Mechanism of low-temperature selective catalytic reduction of NO with NH$_3$ over carbon-supported Mn$_3$O$_4$: Role of surface NH$_3$ species: SCR mechanism. *J. Catal.* **2004**, *226*, 138–155. [CrossRef]

47. Jiang, C.; Zhang, X.; Jia, D.; Song, L. Performance of Hβ zeolites modified by Ce$^{3+}$ on synthesis of ethyl anthrquinone. *J. China. Univ. Petrol. Nat. Sci.* **2015**, *39*, 151–156.

48. Liu, Z.; Zhang, S.; Li, J.; Ma, L. Promoting effect of MoO$_3$ on the NO$_x$ reduction by NH$_3$ over CeO$_2$/TiO$_2$ catalyst studied with in situ DRIFTS. *Appl. Catal. B Environ.* **2014**, *144*, 90–95. [CrossRef]

49. Ding, S.; Liu, F.; Shi, X.; He, H. Promotional effect of Nb additive on the activity and hydrothermal stability for the selective catalytic reduction of NO$_x$ with NH$_3$ over CeZrO$_x$ catalyst. *Appl. Catal. B Environ.* **2016**, *180*, 766–774. [CrossRef]

50. Liu, L.; Su, S.; Xu, K.; Li, H.; Qing, M.; Hu, S.; Wang, Y.; Xiang, J. Insights into the highly efficient Co modified MnSm/Ti catalyst for selective catalytic reduction of NO$_x$ with NH$_3$ at low temperature. *Fuel* **2019**, *255*, 115798. [CrossRef]

51. Chen, L.; Li, J.; Ge, M.; Ma, L.; Chang, H. Mechanism of Selective Catalytic Reduction of NO$_x$ with NH$_3$ over CeO$_2$-WO$_3$ Catalysts. *Chin. J. Catal.* **2011**, *32*, 836–841. [CrossRef]

52. Marban, G.; Fuertes, A.B. Kinetics of the low-temperature selective catalytic reduction of NO with NH$_3$ over activated carbon fiber composite-supported iron oxides. *Catal. Lett.* **2002**, *84*, 13–19. [CrossRef]

53. Madia, G.; Koebel, M.; Elsener, M.; Wokaun, A. Side Reactions in the Selective Catalytic Reduction of NO$_x$ with Various NO$_2$ Fractions. *Ind. Eng. Chem. Res.* **2002**, *41*, 4008–4015. [CrossRef]

54. Grossale, A.; Nova, I.; Tronconi, E.; Chatterjee, D.; Weibel, M. The chemistry of the NO/NO$_2$–NH$_3$ "fast" SCR reaction over Fe-ZSM5 investigated by transient reaction analysis. *J. Catal.* **2008**, *256*, 312–322. [CrossRef]

55. Wang, F.; Shen, B.; Zhu, S.; Wang, Z. Promotion of Fe and Co doped Mn-Ce/TiO$_2$ catalysts for low temperature NH$_3$-SCR with SO$_2$ tolerance. *Fuel* **2019**, *249*, 54–60. [CrossRef]

56. Ha, L.; Gao, M.; Feng, C.; Shi, L.; Zhang, D. Fe$_2$O$_3$-CeO$_2$@Al$_2$O$_3$ nanoarrays on Al–Mesh as SO$_2$–tolerant monolith catalysts for NO$_x$ reduction by NH$_3$. *Environ. Sci. Technol.* **2019**, *53*, 5946–5956.

57. Liu, F.; He, H.; Lian, Z.; Shan, W.; Xie, L.; Asakura, K.; Wang, W.; Deng, H. Highly dispersed iron vanadate catalyst supported on TiO$_2$ for the selective catalytic reduction of NO$_x$ with NH$_3$. *J. Catal.* **2013**, *307*, 340–351. [CrossRef]

58. Yao, X.; Zhao, R.; Chen, L.; Du, J.; Tao, C.; Yang, F.; Dong, L. Selective catalytic reduction of NOx by NH$_3$ over CeO$_2$ supported on TiO$_2$: Comparison of anatase, brookite, and rutile. *Appl. Catal. B Environ.* **2017**, *208*, 82–93. [CrossRef]

59. Yu, S.; Lu, Y.; Cao, Y.; Wang, J.; Sun, B.; Gao, F.; Tang, C.; Dong, L. Composite catalytic systems: A strategy for developing the low temperature NH$_3$–SCR catalysts with satisfactory SO$_2$ and H$_2$O tolerance. *Catal. Today* **2019**, *327*, 235–245. [CrossRef]

60. Bordeje, E.G.; Pinilla, J.L.; Lazaro, M.J.; Moliner, R. NH$_3$–SCR of NO at low temperatures over sulphated vanadia on carbon coated monoliths: Effect of H$_2$O and SO$_2$ traces in the gas feed. *Appl. Catal. B Environ.* **2006**, *66*, 281–287. [CrossRef]